Spin density wave, Fermi liquid, and fractionalized phases in a theory of antiferromagnetic metals using paramagnons and bosonic spinons

Alexander Nikolaenko,[1] Jonas von Milczewski,[1,2,3] Darshan G. Joshi,[1,4] and Subir Sachdev[1]

[1]*Department of Physics, Harvard University, Cambridge, Massachusetts 02138, USA*
[2]*Max-Planck-Institute of Quantum Optics, 85748 Garching, Germany*
[3]*Munich Center for Quantum Science and Technology, 80799 Munich, Germany*
[4]*Tata Institute of Fundamental Research, Hyderabad 500046, India*

(Received 7 December 2022; revised 21 May 2023; accepted 26 June 2023; published 14 July 2023)

The pseudogap metal phase of hole-doped cuprates can be described by small Fermi surfaces of electronlike quasiparticles, which enclose a volume violating the Luttinger relation. This violation requires the existence of additional fractionalized excitations which can be viewed as fractionalized remnants of the paramagnon. We fractionalize the paramagnon into the bosonic spinons of the spin liquid described by the $\mathbb{CP}^1$ U(1) gauge theory, and we present a gauge theory of the bosonic spinons, a Higgs field, and an ancilla layer of fermions coupled to the original electrons. Along with the small Fermi surface pseudogap metal, this theory displays conventional phases: the large Fermi surface Fermi liquid with a low-energy paramagnon mode, and phases with spin density wave order. We describe the evolution of the electronic photoemission spectrum across these quantum phase transitions. We consider both the two-sublattice Néel and incommensurate spin density wave phases, and we find that the latter has spiral spin correlations.

DOI: 10.1103/PhysRevB.108.045123

I. INTRODUCTION

Paramagnons are central actors in the theory of magnetism in Fermi liquids [1,2]: they are collective spin excitations with spin $S = 1$, Landau-damped by their coupling to gapless particle-hole excitations across the Fermi surface. Exchange of ferromagnetic paramagnons is believed to lead to superfluidity in ^{3}He [3], and exchange of antiferromagnetic paramagnons is argued to lead to superconductivity with unconventional spin-singlet pairing in numerous correlated electron compounds [4,5].

The application of the paramagnon theory to hole-doped cuprates faces a challenge from the experimentally observed pseudogap metal regime at low hole doping away from the insulating antiferromagnet at half-filling. This is a metallic phase with no long-range magnetic order in which the conventional Luttinger-volume Fermi surface is partially gapped, displaying only "Fermi arcs" in the photoemission spectrum [6–10]. In many theoretical approaches, including the one followed in the present paper, the pseudogap metal is postulated to have small "hole pocket" Fermi surfaces of size p, where p is the hole-doping density (there is photoemission [11] and angle-dependent magnetoresistance [12] evidence for such pockets). Such a pseudogap metal appeared early on in Ref. [13], in a theory of fluctuating paramagnons in a doped antiferromagnet. This metallic state, if continued to zero temperature (T), does not obey the Luttinger theorem on the volume enclosed by the Fermi surface, which states that the Fermi surface of holes must have size $1 + p$ (or a Fermi surface of electrons must have size $1 - p$). It was argued [14,15] that violations of the Luttinger theorem in such a metal, hereafter called FL* in this paper, require the presence of fractionalization and emergent gauge fields: in particular, any such metallic state must have deconfined, charge 0, spin $S = 1/2$ excitations ("spinons"). These spinons are distinct from the quasiparticle excitations around the Fermi surface of holes, which have charge $+e$ and spin 1/2. The theory of Ref. [13] was extended to a complete theory of the FL* metal in Refs. [16–19] by fractionalizing the O(3) paramagnon field $\boldsymbol{n} \equiv n^a$ ($a = x, y, z$ is a spin index) in a $\mathbb{CP}^1$ representation [20,21] by

$$\boldsymbol{n} = w^*_\alpha \boldsymbol{\sigma}^\alpha_\beta w^\beta. \tag{1.1}$$

Here w^β are the required bosonic spinons, with $\alpha, \beta = \uparrow, \downarrow$ $S = 1/2$ spin indices, and $\boldsymbol{\sigma}$ are the Pauli matrices (we also note a theory of the FL* state using fermionic spinons [22]). Note that (1.1) introduces a U(1) gauge invariance, and the resulting U(1) photon is the emergent photon of the FL* metal. The monopoles in this U(1) gauge field carry Berry phases [20,21], and this extends the range of deconfinement [23,24]. In this paper, we will obtain our effective theory of paramagnons and spinons by employing the recently developed ancilla qubit method to describe the FL* metal and the phases in its vicinity [25–28]. (We note the approach of Ref. [19] in which the electron is not fractionalized, and the pseudogap metal is obtained by interactions between electrons and bosonic spinons—we will connect here to this approach in Sec. IV C. We also note other approaches [29–32] using ancilla degrees of freedom.) An earlier paper [28] has shown that the ancilla method provides a good fit to the photoemission spectrum in the hole-doped cuprates in both the nodal and antinodal regions of

 ©2023 American Physical Society

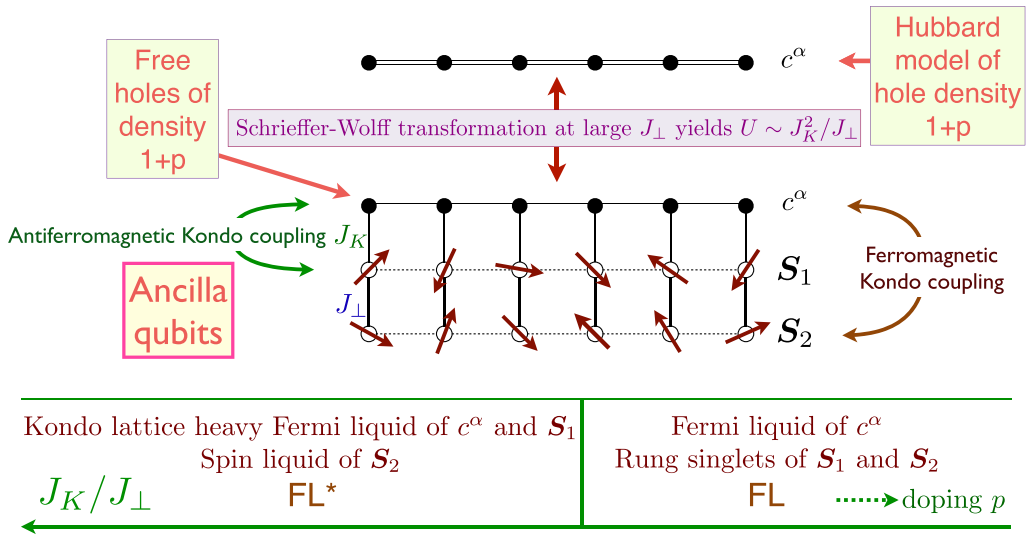

FIG. 1. Schematic illustration of the ancilla theory of the single-band Hubbard model [25–28]. A canonical transformation, which can be carried out order-by-order in $J_\perp$, maps free electrons (c^α) coupled to a bilayer antiferromagnet (with $S = 1/2$ spins $\boldsymbol{S}_1, \boldsymbol{S}_2$ in the two layers, respectively) to a Hubbard model for c^α with on-site repulsion U. In the present paper, we employ fermionic spinons to describe the $\boldsymbol{S}_1$ spins, and bosonic spinons to describe the $\boldsymbol{S}_2$ spins.

the Brillouin zone, including a description of the momentum and energy dependence of the line shapes in the antinodal region.

The ancilla method can be viewed as a simple and foolproof way of obtaining an effective low-energy theory consistent with all symmetries, anomalies, and Luttinger relations. The basic idea of this method is recalled in Fig. 1. First, as shown in Appendix A of Ref. [27], we use an inverse Schrieffer-Wolff transformation to transform the single-band Hubbard model to a model of noninteracting electrons coupled via Kondo coupling J_K to a bilayer antiferromagnet of ancilla spins with rung-exchange $J_\perp$: at large $J_\perp$, the ancilla spins form rung singlets, and accounting for the virtual rung triplet excitations leads to a Hubbard model for the electrons with $U \sim J_K^2/J_\perp$. The first ancilla layer has an antiferromagnetic Kondo coupling J_K to the noninteracting electrons, while the second ancilla layer has an effective ferromagnetic Kondo coupling. The FL* phase is obtained when we assume that the antiferromagnetic Kondo coupling scales to strong coupling (as it does in the Kondo impurity problem) and dominates over $J_\perp$. Then we obtain the heavy Fermi liquid state of the Kondo lattice formed by the c^α layer and the $\boldsymbol{S}_1$ spins: this state has total hole density $1 + p + 1 = p \,(\mathrm{mod}\, 2)$, and thus it yields hole pockets of size p. Meanwhile, the $\boldsymbol{S}_2$ spins with ferromagnetic Kondo couplings cannot be ignored: the ferromagnetic Kondo coupling scales to weak coupling, and so we can safely assume that the $\boldsymbol{S}_2$ spins decouple from the conduction electrons and form a spin liquid, which provides the neutral spinon excitations and the associated emergent gauge fields required in the FL* state. In summary, this theory of the pseudogap metal can be described by the following slogan:

> Pseudogap Metal =
> Kondo Lattice Heavy Fermi Liquid $\oplus$ Spin Liquid.

A cartoon view of the paramagnon fractionalization approach is presented in Fig. 2(a). The previous studies in the ancilla method [25–28] have used fermionic spinons to describe the spin liquid in the $\boldsymbol{S}_2$ spins. In the present paper, we shall use bosonic spinons to describe the spin liquid such as that realized by the $\mathbb{CP}^1$ U(1) gauge theory [20,21,33], as in (1.1). Given the many dualities between the bosonic and fermionic spinon approaches [34–36], we expect there is a nonperturbative mapping between the results obtained by the two approaches. But at the level of mean-field theory, and perturbative fluctuations, the results can be quite different, and much insight is gained by comparisons between them. Our study of the fermionic spinon dual description of the $\mathbb{CP}^1$ U(1) spin liquid is presented in a companion paper [37]: the dual has fermionic spinons moving in π flux coupled to a SU(2) gauge field [34].

The mechanics by which the ancilla method delivers hole pocket Fermi surfaces of size p has similarities to the "hidden" fermion approaches with zeros in the electron Green's function [38–52] and "YRZ" [53,54] approaches. In all cases, the electron has a self-energy which is similar to the propagator of fermions in an auxiliary band; in the ancilla method, the auxiliary fermions reside on the first ancilla layer. The spinon excitations arising from the second ancilla layer are

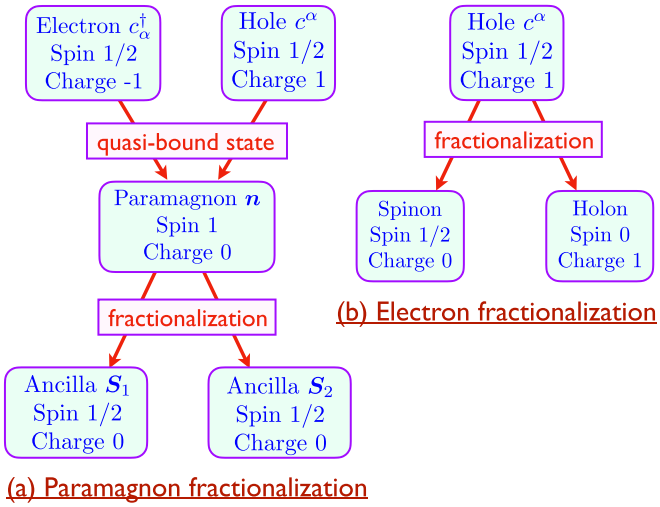

FIG. 2. Comparison of the paramagnon and electron fractionalization approaches. For the $t \gg J$ regime of the t-J model description of the single-band Hubbard model, the holon is unlikely to survive as a fractionalized excitation, and there is no clear experimental evidence for it. All charge carriers have spin $S = 1/2$ in the paramagnon fractionalization approach employed in the present paper. We use the fermions f^p to describe the ancilla spins $\boldsymbol{S}_1$ and bosons Z^p to describe the ancilla spins $\boldsymbol{S}_2$.

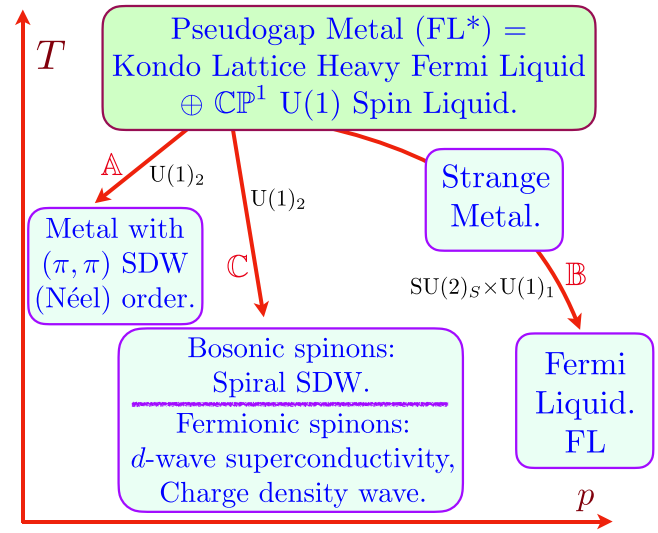

FIG. 3. Schematic of quantum phases in a temperature (T) and doping (p) phase diagram for the hole-doped cuprates. In this paper, we view the FL* pseudogap metal as the "parent," from which various low-T phases without fractionalization follow via confining or Higgs transition. The confinement/Higgs transitions along $\mathbb{A}$, $\mathbb{B}$, $\mathbb{C}$ are discussed in the text; also indicated are the primary gauge groups from Table I which drive these transitions. Along arrow $\mathbb{C}$, the bosonic spinon approach [20,21,33] yields only a spiral SDW, as we shall see in Sec. V. The dual fermionic spinon approach to the *same* spin liquid employs fermions moving in π flux coupled to a SU(2) gauge field [34], and its confinement along $\mathbb{C}$ is described in Ref. [37], yielding d-wave superconductivity and charge density wave order.

not explicitly present in these earlier theories, but it has been argued [50–52,55] that a similar role is played by the zeros of the electron Green's function. The zeros contribute a linear in T specific heat and constant spin susceptibility [50–52] in a manner similar to the mean-field theory of a spinon Fermi surface in a U(1)-FL* state. However, when we include the gauge fluctuations in the U(1)-FL* theory, the resulting $T^{2/3}$ specific heat is not captured by the theory of Green's function zeros.

Along with providing a description of the pseudogap metal as an FL* phase, the bosonic spinon approach of the present paper allows us to address confinement transitions of the fractionalized metal. It is relatively easy to reach the spin density wave (SDW) metallic state with Néel antiferromagnetic order at smaller p; we simply condense the w^α spinon [56], as along arrow $\mathbb{A}$ in Fig. 3. This simultaneously breaks spin and translational symmetries in the appropriate manner, and also Higgses out the U(1) photon so that no fractionalized excitations remain. If the w^α condensate is at zero wave vector, the spin density wave phase has conventional Néel order at wave vector (π, π). However, the coupling to the charge carriers can also induce a w^α condensate at a nonzero wave vector (as along arrow $\mathbb{C}$ in Fig. 3), leading to incommensurate spin density wave states, as we shall discuss in Sec. V. We will describe the evolution of the Fermi surfaces from the FL* state to these SDW states. A significant result of our analysis is that the nonzero wave-vector condensation of the w^α spinons of the $\mathbb{CP}^1$ U(1) spin liquid leads to a spiral SDW, and not to the collinear SDW associated with "stripe" states.

The transition from the FL* metal to the Luttinger-volume Fermi liquid phase (hereafter denoted FL) at larger p cannot be described in such a facile manner. One of the purposes of this paper is to complete the phase diagram of this bosonic spinon approach to the FL* state, and also connect the FL phase to the FL* and SDW phases. The confinement transition from FL* to the Luttinger-theorem-obeying Fermi liquid (along arrow $\mathbb{B}$ in Fig. 3) is quite involved, and proceeds via a rather exotic intermediate metallic phase D, as shown in Fig. 4.

We note in passing that there are numerous other approaches to the pseudogap metal (e.g., Refs. [55,57–63])

TABLE I. Transformations of the main fields under gauge $[U(1)_1, U(1)_2, SU(2)_S]$ and global $[U(1)_g, SU(2)_g]$ symmetries. Listed are the charges under the U(1) symmetries, and the dimensions of the representations under the SU(2) symmetries in boldface. The effective action for the c^α (the gauge-invariant electrons), f^p (spinons in the first ancilla layer), Z^p (spinons in the second ancilla layer), and Φ^p_α (Higgs field hybridizing the electrons with the first ancilla layer) is obtained by obeying these symmetries, and it forms the basis of our results. The paramagnon field n^a is a composite of the Z^p and Φ^p_α as defined in (2.6).

Field	Statistics	$U(1)_1$	$U(1)_2$	$SU(2)_S$	$U(1)_g$	$SU(2)_g$
c^α	fermion	0	0	**1**	1	**2**
f^p	fermion	1	0	**2**	0	**1**
Z^p	boson	0	1	**2**	0	**1**
Φ^p_α	boson	1	0	**2**	-1	$\bar{\mathbf{2}}$
n^a	boson	0	0	**1**	0	**3**

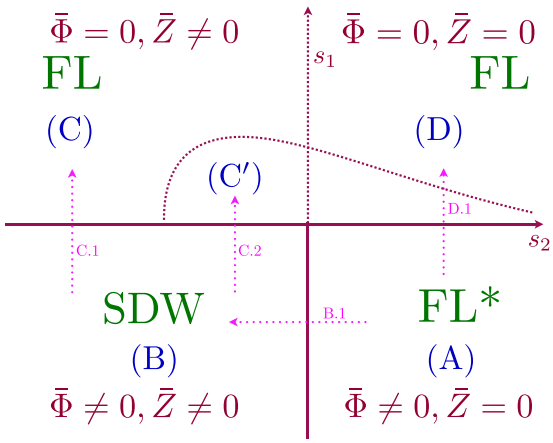

FIG. 4. Mean-field phase diagram of (4.1) for $w_1 + w_2 = 0$. The fermion spectrum and gauge fluctuations in the phases are described in Secs. IV A–IV D. The Fermi surface evolution along the dotted arrows is described in the labeled subsections of Sec. IV. Region C′ has a large c^α Fermi surface (as in the FL phase), along with small pocket ghost Fermi surfaces and emergent $[\mathrm{U}(1)_1 \times \mathrm{U}(1)_d]/\mathbb{Z}_2$ gauge fields. The boundary of C′ is vertical and s_1-independent in mean-field theory, but we have sketched a curved boundary to connect with the possible ghost Fermi surfaces in region D. Most of region D is also expected to be FL, apart from at or near the transition to FL*, where a large ghost Fermi surface may appear along with emergent $[\mathrm{U}(1)_1 \times \mathrm{SU}(2)_S]/\mathbb{Z}_2$ gauge fields [25]. The quantum phase transition(s) along arrow D.1 has been discussed in earlier work [25,26].

which begin by fractionalizing the electron into a charge $+e$ spin $S = 0$ "holon," and a spinon, as in Fig. 2(b). The main difficulty with these approaches is that they do not naturally lead to an FL* metal. In the case in which the holon is a fermion, the mean-field description in such approaches leads to a "holon metal," with a Fermi surface of charge $+e$ spin $S = 0$ quasiparticles. A Fermi surface of "holes" rather than "holons" can then be obtained by arguing that the holons form bound states with the spinons to yield charge $+e$ spin $S = 1/2$ quasiparticles, as in the FL* metal. In practice, however, this binding process is difficult to carry out with any degree of control. Furthermore, there is no clear experimental evidence for the existence of spinless charge carriers in any energy regime in the cuprates. Therefore, we avoid such electron fractionalization approaches in the present paper, and will only fractionalize the paramagnon, as in (1.1).

Section II describes the structure of the gauge theory of the ancilla approach, as summarized in Table I. Section III presents the effective action, obtained by imposing the symmetries in Table I. The mean-field phase diagram is obtained in Sec. IV for the case of (π, π) SDW order, along with results on the evolution of the Fermi surfaces across the quantum phase transitions. Section V extends our results to SDW ordering at other wave vectors.

II. EMERGENT GAUGE STRUCTURE

The ancilla approach has an intricate structure of gauge charge assignments, and the resulting gauge theory is the main tool used to derive the effective actions we shall work with below. This structure can be understood simply from rather general arguments, as we now show.

TABLE II. As in Table I, for auxiliary fields used at intermediate stages.

Field	Statistics	$\mathrm{U}(1)_1$	$\mathrm{U}(1)_2$	$\mathrm{SU}(2)_S$	$\mathrm{U}(1)_g$	$\mathrm{SU}(2)_g$
ψ^α	fermion	1	0	**1**	0	**2**
w^α	boson	0	1	**1**	0	**2**
$H^{a\ell}$	boson	0	0	**3**	0	**3**

First, we have the U(1) gauge charges carried by the bosonic spinons w^α of the second ancilla layer in (1.1). We refer to this as $\mathrm{U}(1)_2$. See Table II below.

We will continue to use a fermionic spinon (ψ^α) representation of the spins in the first ancilla layer

$$\boldsymbol{S}_1 = \tfrac{1}{2} \psi^\dagger_\alpha \boldsymbol{\sigma}^\alpha_\beta \psi^\beta. \tag{2.1}$$

This introduces a U(1) gauge invariance, which we will denote $\mathrm{U}(1)_1$. [Actually, the full gauge invariance of (2.1) is SU(2) [64], but we will always work with spin liquids in which the SU(2) is Higgsed down to U(1), and so we ignore this feature.] See Table II below.

Finally, we need an $\mathrm{SU}(2)_S$ gauge field to impose the rung spin-singlet structure of the ancilla layers, induced by the large $J_\perp$. This is realized by transforming to a rotating reference frame in spin space [65]. The spin-singlet projection requires that we perform the same SU(2) rotation $\mathcal{R}$ in both ancilla layers. So we introduce fermions f^p and bosons Z^p ($p = \pm$) by the transformation

$$\begin{pmatrix} \psi^\uparrow \\ \psi^\downarrow \end{pmatrix} = \mathcal{R} \begin{pmatrix} f^+ \\ f^- \end{pmatrix}, \quad \begin{pmatrix} w^\uparrow \\ w^\downarrow \end{pmatrix} = \mathcal{R} \begin{pmatrix} Z^+ \\ Z^- \end{pmatrix}. \tag{2.2}$$

The fields f^p and Z^p now both carry a fundamental $\mathrm{SU}(2)_S$ gauge charge. In addition, as is clear from (2.2), f^p carries a $\mathrm{U}(1)_1$ gauge charge, and Z^p carries a $\mathrm{U}(1)_2$ gauge charge. These charge assignments are summarized in Table I. The monopoles in $\mathrm{U}(1)_2$ will carry Berry phases [20,21].

These gauge charges combine to yield a $[\mathrm{U}(1)_1 \times \mathrm{U}(1)_2 \times \mathrm{SU}(2)_S]/\mathbb{Z}_2$ gauge theory [25,26], some of whose phases we will study below. Note that the subscripts of the symmetry groups are just identifying labels, and they do *not* refer to a Chern-Simons level.

In addition to the gauge charge assignments, we should also keep track of the global symmetries of charge and spin conservation. These we label as $\mathrm{U}(1)_g$ and $\mathrm{SU}(2)_g$. We present the global charge assignments of all the fields introduced so far in Tables I and II.

The theory presented here requires one more boson which connects the global and gauge symmetries. This boson is the analog of the hybridization boson of the Kondo lattice, whose condensation yields the Kondo effect and the heavy Fermi liquid state [66–69]. Here, the required boson is a complex four-component Higgs field Φ^p_α [25,26]. This hybridizes the fermions in the first ancilla layer with the electrons in the top layer, and so we have the operator correspondence

$$\Phi^p_\alpha \sim c^\dagger_\alpha f^p. \tag{2.3}$$

The gauge and global transformation properties of Φ_α^p can be easily deduced from (2.3), and they are listed in Table I. As discussed in Ref. [25], the boson Φ_α^p can be explicitly obtained from a Hubbard-Stratonovich transformation of the Kondo interaction between the electrons and the first ancilla layer.

Analogous to the Higgs field Φ_α^p, which connects the fermions c^α and f^p, it might seem we need another Higgs field to connect the $SU(2)_g$ spin space of w^α [as defined by (1.1)] to the $SU(2)_S$ pseudospin space of Z^p. By taking the $U(1)_2$ gauge-invariant combination of the Z^p, we can introduce such a Higgs field $H^{a\ell}$ ($\ell = 1, 2, 3$, $a = x, y, z$) with 3×3 real components:

$$n^a = w_\alpha^* \, \sigma_\beta^{a\alpha} \, w^\beta \sim H^{a\ell} Z_p^* \, \sigma_{p'}^{\ell p} Z^{p'}, \tag{2.4}$$

where σ^ℓ are also the Pauli matrices. Again, the gauge and global charges for $H^{a\ell}$ can be deduced from Table II. However, these symmetry properties also show that we can identify the Higgs field $H^{a\ell}$ as the "square" of the Higgs field Φ_α^p,

$$H^{a\ell} = \Phi_\alpha^p \, \Phi_{p'}^{*\beta} \, \sigma_\beta^{a\alpha} \sigma_p^{\ell p'}. \tag{2.5}$$

Consequently, we will not need to include $H^{a\ell}$ as an independent field in our considerations, and just identify it as in (2.5). Also, we can combine (2.4) and (2.5) to write

$$n^a \sim \Phi_\alpha^p \, \Phi_{p'}^{*\beta} \, \sigma_\beta^{a\alpha} [Z_p^* Z^{p'} - \tfrac{1}{2} \, \delta_p^{p'} \, Z_q^* Z^q], \tag{2.6}$$

which relates the paramagnon field n^a to the Higgs field Φ_α^p and the spinons Z^p.

The remainder of the paper will derive an effective action for the electrons c^α, the fermionic spinons f^p, the bosonic spinons Z^p, and the Higgs field Φ_α^p. This action can largely be deduced from the gauge and symmetry properties listed in Table I. Our results for the phase diagram and the properties of the phases will follow from this effective action.

III. EFFECTIVE ACTION

Our primary assumption is that the structure of the phase diagram is determined primarily by the dynamics of the Higgs fields Z^p and Φ_α^p, and the associated $U(1)_1$, $U(1)_2$, and $SU(2)_S$ gauge fields. In all our discussion here, we will not write out the gauge fields explicitly, as they can be included from the requirements of gauge invariance in a familiar manner. The fermionic matter fields c^α and f^p are also important, and their couplings to the Higgs fields are determined, as usual, by the restrictions of gauge invariance: these couplings then modify the Fermi surfaces, and determining the Fermi surface evolution will be an important focus of our study.

We begin by writing down the form of the Higgs potential, whose minima will determine the structure of the mean-field phase diagram. From Table I we have

$$\begin{aligned} V(Z, \Phi) = {} & s_1 \, \Phi_\alpha^p \Phi_p^{*\alpha} + u_1 \big[\Phi_\alpha^p \Phi_p^{*\alpha}\big]^2 + v_1 \, \Phi_\alpha^p \Phi_\beta^q \Phi_q^{*\alpha} \Phi_p^{*\beta} \\ & + s_2 \, Z_p^* Z^p + u_2 [Z_p^* Z^p]^2 \\ & + w_1 \, Z_p^* Z^p \Phi_\alpha^q \Phi_q^{*\alpha} + w_2 \, Z_p^* Z^q \Phi_\alpha^p \Phi_q^{*\alpha} + \cdots . \end{aligned} \tag{3.1}$$

A variety of minima are possible from such a potential as the "masses" $s_{1,2}$ are varied, but we will limit ourselves to the regime where the minima can be related by gauge and global rotations to

$$\big\langle \Phi_\alpha^p \big\rangle = \bar{\Phi} \, \delta_\alpha^p, \quad \langle Z^p \rangle = (\bar{Z} \, \delta_+^p + \bar{Z}^* \, \delta_-^p)/\sqrt{2}. \tag{3.2}$$

With $\bar{Z} = 0$ and $\bar{\Phi} \neq 0$, such a minimum yields the FL* state, which breaks no global symmetries, and which has been studied in some detail in previous work [25–28]. Our purpose here is to study the remainder of the phase diagram when $\bar{Z}$ is also allowed to be nonzero.

There are also spatial and temporal gradient terms in Z^p and Φ_α^p. But we refrain from writing them out explicitly because they have a familiar form dictated by gauge invariance, and they are not used in the analysis of the present paper. Similarly, there are Maxwell terms for the gauge fields, and monopole Berry phases for the $U(1)_2$ gauge field in the second ancilla layer, which we do not present here [20,21,23,24,34,70].

Finally, let us discuss the fermionic sector, which can also have a significant influence on the fate of fluctuations. As in previous work [25–28], we have the dispersions of the electrons c^α in the physical layer, and the fermions f^p in the first ancilla layer, along with their hybridization (Yukawa) coupling to Φ_α^p:

$$\begin{aligned} H_{cf}^a = & - \sum_{i,j} t_{ij} c_{i\alpha}^\dagger c_j^\alpha + \sum_{i,j} t_{1,ij} f_{ip}^\dagger f_j^p \\ & + \sum_i \big(\Phi_\alpha^p f_{ip}^\dagger c_i^\alpha + \Phi_p^{*\alpha} c_{i\alpha}^\dagger f_i^p \big). \end{aligned} \tag{3.3}$$

Using the Φ condensate in (3.2), H_{cf}^a then yields the fermion dispersion in the FL* phase. Such dispersions were compared with photoemission observations in Ref. [28], and they were able to describe observations well in both the nodal and antinodal regions of the Brillouin zone, and at and away from the Fermi surface. This comparison with data also allowed the determination of the hopping parameters and chemical potentials in t_{ij} and $t_{1,ij}$, and the hybridization $\bar{\Phi}$.

The symmetries in Table I allow a number of additional couplings between the Higgs fields and the fermions (which were not considered in Ref. [28]),

$$\begin{aligned} H_{cf}^b = & -J_s \sum_i \eta_i \, n_i^a \, c_{i\alpha}^\dagger \sigma_\beta^{a\alpha} c_i^\beta + J_\perp \sum_i \eta_i \, f_{ip}^\dagger \sigma_{p'}^{\ell p} f_i^{p'} \, Z_{iq}^* \sigma_{q'}^{\ell q} Z_i^{q'} \\ & + J_3 \sum_i \Big(\eta_i \, f_{ip}^\dagger \sigma_\alpha^{\ell p} \Phi_\beta^\alpha c_i^\beta \, Z_{iq}^* \sigma_{q'}^{\ell q} Z_i^{q'} + \text{H.c.} \Big) \\ & + \lambda \sum_i \Phi_\alpha^p \sigma_\beta^{a\alpha} \Phi_p^{*\beta} \, c_{i\gamma}^\dagger \sigma_\delta^{a\gamma} c_i^\delta, \end{aligned} \tag{3.4}$$

where

$$\eta_i \equiv (-1)^{i_x + i_y} \tag{3.5}$$

is the staggering factor needed because Z^p describes Néel order in the second ancilla layer. More formally, the w^α and Z^p transform nontrivially under lattice symmetries [71], and this implies the presence of η_i. This Néel order is coupled to the electrons c^α via J_s [where n^a is related to Z^p and Φ_α^p as in (2.6)], and to the first layer of ancilla fermions via $J_\perp$. The λ term is proportional to the ferromagnetic moment, and so

it vanishes in mean-field theory in all the phases considered here.

IV. PHASE DIAGRAM

We observe the following steps to describe the phase diagram:

(i) Determine the mean-field phase diagram by minimizing the Higgs potential in (3.1) to obtain the values of $\bar{\Phi}$ and $\bar{Z}$.

(ii) Insert the values of $\bar{\Phi}$ and $\bar{Z}$ into $H^a_{cf} + H^b_{cf}$ in (3.3) and (3.4), and then compute the mean-field dispersions of the fermions and their Fermi surfaces.

(iii) Analyze gauge fluctuations in all the phases and phase transitions so obtained.

We begin by describing the first step above, the mean-field theory of (3.1). With the ansatz (3.2), this becomes the standard Landau theory of tetracritical and bicritical points [72,73], with the Landau potential

$$V(Z,\Phi) = s_1|\bar{\Phi}|^2 + (u_1+v_1)|\bar{\Phi}|^4 + s_2|\bar{Z}|^2 + u_2|\bar{Z}|^4 + (w_1+w_2)|\bar{Z}|^2|\bar{\Phi}|^2. \tag{4.1}$$

We will not work out the phase diagram of (4.1) here, as it is identical to that in early works [72,73]. In the interest of simplicity, we focus on the case $w_1 + w_2 = 0$, when the phase diagram takes the very simple form in Fig. 4. The mean-field theory yields four phases, A, B, C, and D, separated by phase boundaries at $s_1 = 0$ or $s_2 = 0$. These phases are discussed below in the correspondingly named subsections. Upon including gauge fluctuations, phases C and D ultimately become conventional Fermi liquids (FL) with a single large Fermi surface of the c^α fermions, so phases C and D can be smoothly connected without an intervening quantum phase transition, and this is indicated by making the line $s_2 = 0$, $s_1 > 0$ a dashed line. However, within regions C and D, below the curved dotted line, there is the possibility of additional "ghost" Fermi surfaces of the f^p fermions [25,26]; these ghost Fermi surfaces will be small for $s_2 < 0$, and large for $s_2 > 0$.

A. FL*

This phase has $\bar{\Phi} \neq 0$, $\bar{Z} = 0$. The Φ^p_α condensate fully Higgses the $SU(2)_S$ and $U(1)_1$ gauge fields, but the $U(1)_2$ gauge field remains potentially deconfined.

With $\bar{Z} = 0$, the situation here is as described in earlier papers [25–28], and also along the eventual transition to a Fermi liquid in region D. So we obtain small hole pocket Fermi surfaces of size p, a deconfined $U(1)_2$ gauge field.

The bosonic spinon description of the spin liquid in the second ancilla layer can make a potential difference here from the earlier work: the $U(1)_2$ spin liquid can have a monopole-induced confinement to a valence bond solid at some large length scale. Alternatively, a stable $\mathbb{Z}_2$ spin liquid can appear here [23,24,34,70].

B. SDW

This phase has $\bar{\Phi} \neq 0$, $\bar{Z} \neq 0$. Now the Φ^p_α and Z^p condensates fully Higgs all the $SU(2)_S$, $U(1)_1$, and $U(1)_2$ gauge fields, and there are no deconfined gauge charges. However, the presence of both Higgs condensates implies that $\langle \boldsymbol{n} \rangle \neq 0$ from (2.6), and the global symmetry $SU(2)_g$ is broken, implying the presence of SDW order.

1. Fermi surfaces from FL to SDW*

Here we follow arrow $\mathbb{A}$ in Fig. 3, or arrow B.1 in Fig. 4. To compute Fermi surfaces, we start from the mean-field Hamiltonian in the reduced Brillouin zone, $H = \sum_{\vec{k}} \psi^\dagger_{\vec{k}} H_{\vec{k}} \psi_{\vec{k}}$, where $\psi_{\vec{k}} = (c_{\vec{k}}, c_{\vec{k}+\vec{Q}_\pi}, f_{\vec{k}}, f_{\vec{k}+\vec{Q}_\pi})$, $\vec{Q}_\pi = (\pi, \pi)$, and (with $\bar{\Phi}$, $\bar{Z}$ real)

$$H_{\vec{k}} = \begin{pmatrix} \epsilon_{c\vec{k}} & J_s\bar{Z}^2\bar{\Phi}^2 & \bar{\Phi} & 0 \\ J_s\bar{Z}^2\bar{\Phi}^2 & \epsilon_{c\vec{k}+\vec{Q}_\pi} & 0 & \bar{\Phi} \\ \bar{\Phi} & 0 & \epsilon_{f\vec{k}} & J_\perp\bar{Z}^2 \\ 0 & \bar{\Phi} & J_\perp\bar{Z}^2 & \epsilon_{f\vec{k}+\vec{Q}_\pi} \end{pmatrix}. \tag{4.2}$$

With the input of the variations in the values of $\bar{\Phi}$ and $\bar{Z}$ across the phase diagram of Fig. 4, this Hamiltonian describes the mean-field evolution of the Fermi surfaces across all the phases. The eigenvalues of $H_{\vec{k}}$ cannot be found analytically for nonzero $\bar{Z}$ and $\bar{\Phi}$, but it is easy to diagonalize the Hamiltonian numerically. We choose $J_s = J_\perp = 1$ and tight-binding parameters consistent with experimental ARPES observations in Bi2201 [7]:

$$\epsilon_{c\vec{k}} = -2t(\cos k_x + \cos k_y) - 4t'\cos k_x \cos k_y - 2t''(\cos 2k_x + \cos 2k_y) - 4t'''(\cos 2k_x \cos k_y + \cos 2k_y \cos k_x) - \mu_c, \tag{4.3}$$

where $t = 0.22, t' = -0.034, t'' = 0.036, t''' = -0.007, \mu_c = -0.24$ and

$$\epsilon_{f\vec{k}} = 2t_1(\cos k_x + \cos k_y) + 4t'_1\cos k_x \cos k_y + 2t''_1(\cos 2k_x + \cos 2k_y) - \mu_f, \tag{4.4}$$

where $t_1 = 0.1, t'_1 = -0.03, t''_1 = -0.01, \mu_f = 0.009$. Chemical potentials will vary in order to satisfy constraints $\langle c^\dagger_{i\alpha} c^\alpha_i \rangle = (1-p)/2$ and $\langle f^\dagger_{ip} f^p_i \rangle = 1/2$, while we will use the same tight-binding parameters in the rest of the paper. We also compute spectral weights by taking the imaginary part of the retarded Green's function with finite imaginary broadening $\delta = 0.01$. The spectral weight, contrary to a Fermi surface, is directly measured in ARPES experiments. Figure 5 shows the Fermi surface and spectral weight in the FL* phase. There are eight hole pockets instead of four since the Brillouin zone is shrunk by two in our basis, but the spectral weight only sees four hole pockets.

As we move into the SDW phase along the B.1 line, eight hole pockets turn into four hole pockets, as shown in Fig. 6. Unlike the FL* pockets in Fig. 5, these pockets are symmetric with respect to the boundaries of the reduced Brillouin zone (black dashed line). Moreover, their area enclosed in the original Brillouin zone has doubled [60]. These are features that should be possible to detect in experiment.

The transition is described by a $\mathbb{CP}^1$ field theory for the $U(1)_2$ gauge field coupled to Z^p, along with spectator bands of fermions neutral under $U(1)_2$; recall that the monopoles in $U(1)_2$ do carry Berry phases, and this allows deconfined criticality [23,24].

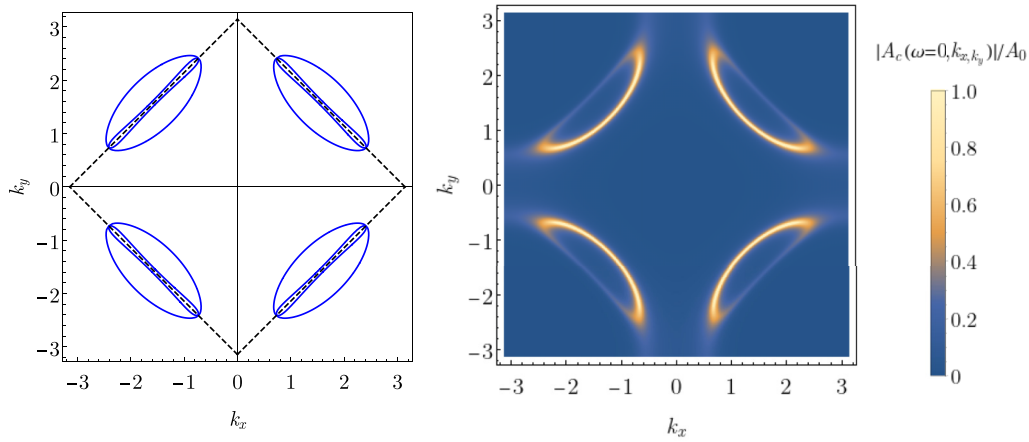

FIG. 5. Fermi surface and spectral weight in the FL* phase. Parameters: $\bar{\Phi} = 0.09$, $\bar{Z} = 0.0$, $\mu_c = -0.243$, $\mu_f = 0.009$.

C. FL

This phase has $\bar{\Phi} = 0$, $\bar{Z} \neq 0$. The Z^p condensate breaks the $[SU(2)_S \times U(1)_2]/\mathbb{Z}_2$ gauge symmetry down to a diagonal U(1) symmetry, which we refer to as $U(1)_d$: this is the linear combination of $U(1)_2$ and the x component of $SU(2)_S$, which leaves the second equation in (3.2) invariant (for real $\bar{Z}$). The $U(1)_1$ gauge field is also potentially deconfined. The f^p Fermi surface can be gapped via the $J_\perp$ coupling in (3.4) and (4.2) provided the Z^p condensate is large enough. We assume the f^p fermions are gapped for now, and consider the situation with gapless f^p excitations below. With the f^p fermions gapped, the Polyakov mechanism of monopole proliferation can confine $[U(1)_1 \times U(1)_d]/\mathbb{Z}_2$ gauge fields, but we do need to consider the monopole Berry phases to determine the scales over which deconfinement can survive [20,21,23,24]. Upon confinement, the Higgs field Φ^p_α is no longer an elementary excitation in the FL phase. The gauge-neutral two-particle bound state of Φ^p_α turns into the paramagnon via (2.6). For the explicit form of (2.6) here, it is useful to orient the Z^p condensate in the z direction by replacing (3.2) by $\langle Z^p \rangle = \bar{Z}\,\delta^p_+$; then (2.6) becomes

$$\begin{aligned} \boldsymbol{n} &\sim \Phi^+_\alpha \boldsymbol{\sigma}^\alpha{}_\beta \Phi^{*\beta}_+ - \Phi^-_\alpha \boldsymbol{\sigma}^\alpha{}_\beta \Phi^{*\beta}_-, \\ \boldsymbol{m} &\sim \Phi^+_\alpha \boldsymbol{\sigma}^\alpha{}_\beta \Phi^{*\beta}_+ + \Phi^-_\alpha \boldsymbol{\sigma}^\alpha{}_\beta \Phi^{*\beta}_-. \end{aligned} \tag{4.5}$$

We have also noted the form of the ferromagnetic order parameter $\boldsymbol{m}$, which follows from the λ coupling in (3.4). The Φ^p_α now carry charge p under $U(1)_d$, and charge 1 under $U(1)_1$. We can realize a theory without ferromagnetism, $\boldsymbol{m} \approx 0$, by condensing $\varepsilon^{\alpha\beta}\Phi^+_\alpha \Phi^-_\beta$ so that $\Phi^-_\alpha \sim \varepsilon_{\alpha\beta}\Phi^{\beta *}_+$. This condensate Higgses $U(1)_1$, but there remains the possibility that $U(1)_d$ is deconfined over a significant length scale, in which case we should consider the theory with fractionalized Φ^+_α excitations: such a theory reduces to that considered in Sec. III of Ref. [19] with the bosonic spinon z^*_α of that paper corresponding to our Φ^+_α. However, note that the spinons of Φ^+_α represent spin fluctuations on both ancilla layers, and so the Berry phases of the monopoles in $U(1)_d$ *cancel* between the contributions of the two layers, and do not suppress confinement [23,24]. Once $U(1)_d$ confines, we obtain the usual Hertz theory [74] of a paramagnon $\boldsymbol{n} \sim \Phi^+_\alpha \boldsymbol{\sigma}^\alpha{}_\beta \Phi^{*\beta}_+$ coupled to large Fermi surface. The deconfined theory in terms of the Φ^+_α has no monopoles/hedgehogs, and so it only includes orientational fluctuations of the SDW order, whereas the $\boldsymbol{n}$ theory also allows amplitude fluctuations.

For a smaller Z^p condensate, the f^p fermions can be gapless because pocket f^p ghost Fermi surfaces will survive, and we have indicated this region of the phase diagram as C′ in Fig. 4. With gapless f^p fermions, the Polyakov mechanism for

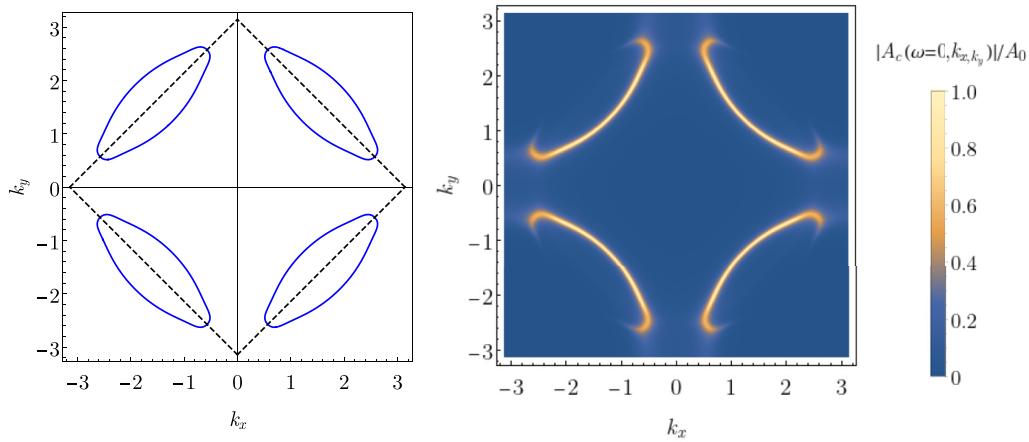

FIG. 6. Fermi surface and spectral weight in the SDW phase. Parameters: $\bar{\Phi} = 0.09$, $Z = 0.2$, $\mu_c = -0.237$, $\mu_f = 0.006$.

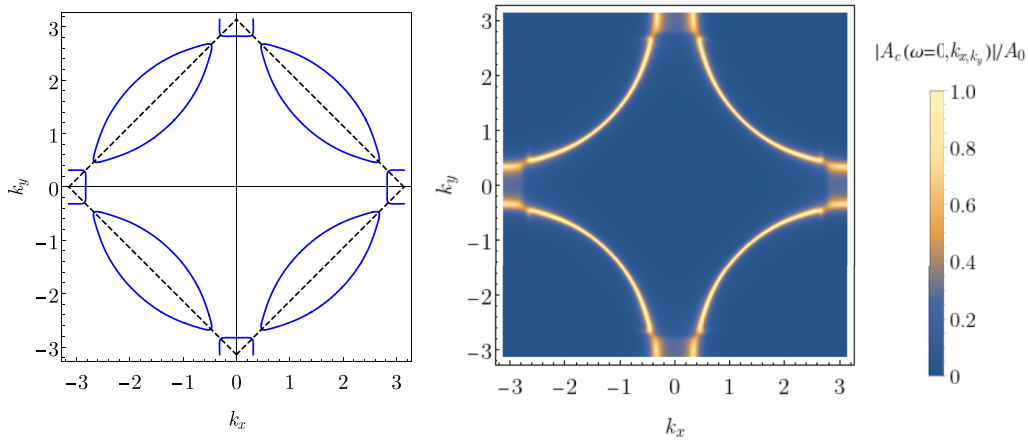

FIG. 7. Fermi surface and spectral weight in the SDW phase, close to FL phase. Parameters: $\Phi = 0.03, Z = 0.2, \mu_c = -0.210, \mu_f = 0.062$.

confinement is suppressed [75]. The f^p fermions have gauge charges $p = \pm$ under $U(1)_d$, and the same gauge charge under $U(1)_1$: consequently, there is a near-cancellation of attractive and repulsive forces [26], and it is possible that the pocket f^p Fermi surfaces will avoid a pairing instability. If the pairing instability does occur, the ancilla layers become trivial, and we obtain a conventional FL state—the $[U(1)_1 \times U(1)_d]/\mathbb{Z}_2$ gauge symmetry is Higgsed down to $U(1)_d$, and the fermion gap will lead to the $U(1)_d$ confinement discussed above.

1. Fermi surfaces from SDW to FL

The transition from SDW to Fermi liquid (along the C.1 line) is shown in Fig. 7. As we move closer to FL phase, electron pockets appear at the antinodal points, and Fermi arcs evolve into a usual Fermi surface of a Fermi liquid.

The f^p electron Fermi surface is gapped, and so as discussed above, the transition is a conventional transition [74] from SDW to FL, with the J_s term in (3.4) coupling to the SDW order parameter, the paramagnon $\boldsymbol{n}$ defined by (4.5).

2. Fermi surfaces from SDW to C′

The transition between SDW and C′ phase happens when $\bar{Z}$ is smaller and the Fermi surface of f^p fermions is not gapped. Figure 8 shows a c^α fermion Fermi surface (blue line), and an f^p fermion Fermi surface (red line). However, spectral weight lies only on the physical electron Fermi surface.

Assuming the $[U(1)_1 \times U(1)_d]/\mathbb{Z}_2$ gauge fields are deconfined, the transition is described by a gauge theory for the Φ^p_α and the fermions; for $\langle Z^p \rangle = \bar{Z}\,\delta^p_+$, the Φ^p_α and f^p carry gauge charges p under $U(1)_d$ and 1 under $U(1)_1$. The monopoles in both U(1)'s are suppressed by the f^p Fermi surfaces, and they do not carry Berry phases because the Φ^p_α represent spin fluctuations in a bilayer antiferromagnet.

D. Ghost Fermi surfaces

1. Fermi surfaces from FL to D*

The transition between FL* and D was studied in previous works [25–28] and describes an emergence of hole pockets from the full Fermi surface; see Fig. 9.

V. INCOMMENSURATE SPIN DENSITY WAVES

This section will explore the possibility that the SDW phase in Fig. 4 has incommensurate spin correlations, as indicated as a possibility along arrow $\mathbb{C}$ in Fig. 3. This is motivated by the numerous observations of incommensurate spin order in the underdoped regime of the La-based cuprates.

We approach the SDW phase B from the FL* phase A. Both of these phases have the Higgs condensate $\langle \Phi^p_\alpha \rangle \neq 0$, while only the SDW phase has $\langle Z^p \rangle \neq 0$. Our operating assumption is that the coupling to the Fermi pockets of the FL* phases leads the Z^p spinons to condense at an incommensurate wave vector. In the remaining discussion in this section, we will not distinguish between the $SU(2)_S$ indices and the $SU(2)_g$ indices because they are identified by the diagonal Φ^p_α condensate in (3.2). Moreover, the spinons w^α are identified with Z^p by (2.4) and (2.5). So we will denote the spinons by Z^α in this section, and (2.6) becomes

$$n^a = Z^*_\alpha \sigma^{a\alpha}_{\ \beta} Z^\beta. \tag{5.1}$$

We are interested in a state in which the spinon condensate in (3.2) is replaced by

$$\langle Z^\alpha(\vec{r}) \rangle = \bar{Z}^\alpha_1 e^{i\vec{q}_1\cdot\vec{r}} + \bar{Z}^\alpha_2 e^{i\vec{q}_2\cdot\vec{r}} + \bar{Z}^\alpha_3 e^{-i\vec{q}_1\cdot\vec{r}} + \bar{Z}^\alpha_4 e^{-i\vec{q}_2\cdot\vec{r}}, \tag{5.2}$$

where $\vec{q}_1$ and $\vec{q}_2$ incommensurate wave vectors are related by square-lattice symmetries. Thus, we could have $\vec{q}_1 = (\kappa, 0)$ and $\vec{q}_2 = (0, \kappa)$, or we could have $\vec{q}_1 = (\kappa, \kappa)$ and $\vec{q}_2 = (-\kappa, \kappa)$, where κ is some small incommensurate wave vector. Inserting (5.2) into (5.1), we see that the possible ordering wave vectors of the SDW order are

$$(\pi, \pi); \quad (\pi, \pi) \pm 2\vec{q}_1; \ (\pi, \pi) \pm 2\vec{q}_2; \quad (\pi, \pi) \pm \vec{q}_1 \pm \vec{q}_2. \tag{5.3}$$

Of significant importance is the fact that there remains an SDW ordering at the commensurate wave vector (π, π) with weight proportional to

$$\bar{Z}^*_{1\alpha}\sigma^{a\alpha}_{\ \beta}\bar{Z}^\beta_1 + \bar{Z}^*_{2\alpha}\sigma^{a\alpha}_{\ \beta}\bar{Z}^\beta_2 + \bar{Z}^*_{3\alpha}\sigma^{a\alpha}_{\ \beta}\bar{Z}^\beta_3 + \bar{Z}^*_{4\alpha}\sigma^{a\alpha}_{\ \beta}\bar{Z}^\beta_4. \tag{5.4}$$

As the cuprates do not display coexistence between incommensurate SDW and (π, π) Néel ordering, we will only be interested in cases in which (5.4) vanishes for all components

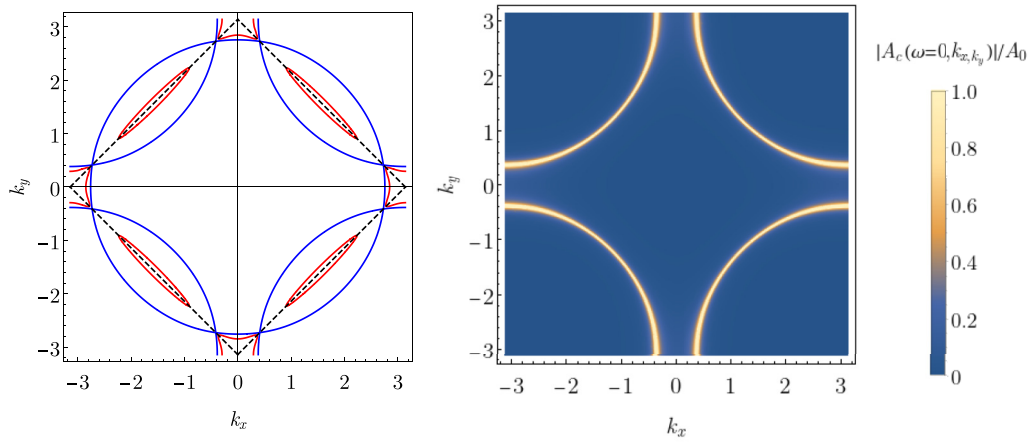

FIG. 8. Fermi surface and spectral weight in the C′ phase. The blue line corresponds to c^α Fermi surface and the red line corresponds to f^p ghost Fermi surface. Parameters: $\Phi = 0.0, Z = 0.1, \mu_c = -0.213, \mu_f = 0.065$.

a. A solution with only a unidirectional SDW at $(\pi, \pi) \pm 2\vec{q}_1$ requires that

$$\bar{Z}^\alpha_{2,4} = 0, \quad \bar{Z}^\alpha_3 = \varepsilon^{\alpha\beta}\bar{Z}^*_{1\beta}. \tag{5.5}$$

Then the SDW ordering is described by

$$\boldsymbol{n}(\vec{r}) = \varepsilon_{\alpha\gamma}\bar{Z}^\gamma_1\, \boldsymbol{\sigma}^\alpha_\beta \bar{Z}^\beta_1\, e^{2i\vec{q}_1\cdot\vec{r}} + \text{c.c.} = (\boldsymbol{m}_1 + i\boldsymbol{m}_2)e^{2i\vec{q}_1\cdot\vec{r}} + \text{c.c.}, \tag{5.6}$$

where $\boldsymbol{m}_{1,2}$ are real vectors obeying

$$\boldsymbol{m}_1\cdot\boldsymbol{m}_1 = \boldsymbol{m}_2\cdot\boldsymbol{m}_2 = \left(\left|\bar{Z}^\alpha_1\right|^2\right)^2, \quad \boldsymbol{m}_1\cdot\boldsymbol{m}_2 = \boldsymbol{0}. \tag{5.7}$$

So we see that (5.6) is a *spiral* SDW, and not a collinear "stripe" SDW. Such spiral SDW states have been considered in many studies, and recently in Ref. [63]. But the present approach of condensing Z^α does not lead to unidirectional "stripe" states with collinear spin correlations, of the type observed in recent numerical studies [76,77].

We now turn to a microscopic mechanism for the condensation of Z^α at an incommensurate wave vector. Our idea is that the coupling of the Z^α to the Fermi pockets of the FL* phase will lead to a Z^α self-energy, and this self-energy will lead to a minimum in the dispersion of the Z^α at $(\pi, \pi) \pm \vec{q}_{1,2}$. A similar approach was used early on in Ref. [13], but in a theory of the paramagnons n^a coupled to the Fermi pockets. Our point here is that the existence of Fermi pockets that do not have a Luttinger volume requires fractionalization, and so we should carry out the computation using the fractionalized spinon excitations Z^α rather than the paramagnons n^a.

We write the Hamiltonian for the electron layer and the first ancilla layer in Eq. (3.3) in the form

$$H_{cf} = \sum_{\vec{k}} \left[\epsilon_{c\vec{k}} c^\dagger_{\vec{k},\alpha} c^\alpha_{\vec{k}} + \epsilon_{f\vec{k}} f^\dagger_{\vec{k},\alpha} f^\alpha_{\vec{k}} + \bar{\Phi} f^\dagger_{\vec{k},\alpha} c^\alpha_{\vec{k}} + \bar{\Phi}^* c^\dagger_{\vec{k},\alpha} f^\alpha_{\vec{k}}\right]. \tag{5.8}$$

This yields the normal fermion Green's functions

$$\begin{aligned} G_c(\vec{k}, i\omega) &= \frac{i\omega - \epsilon_{f\vec{k}}}{(i\omega - \epsilon_{c\vec{k}})(i\omega - \epsilon_{f\vec{k}}) - |\bar{\Phi}|^2} \\ &= \frac{i\omega - \epsilon_{f\vec{k}}}{(i\omega - E_{1\vec{k}})(i\omega - E_{2\vec{k}})}, \end{aligned} \tag{5.9}$$

$$\begin{aligned} G_f(\vec{k}, i\omega) &= \frac{i\omega - \epsilon_{c\vec{k}}}{(i\omega - \epsilon_{c\vec{k}})(i\omega - \epsilon_{f\vec{k}}) - |\bar{\Phi}|^2} \\ &= \frac{i\omega - \epsilon_{c\vec{k}}}{(i\omega - E_{1\vec{k}})(i\omega - E_{2\vec{k}})}, \end{aligned} \tag{5.10}$$

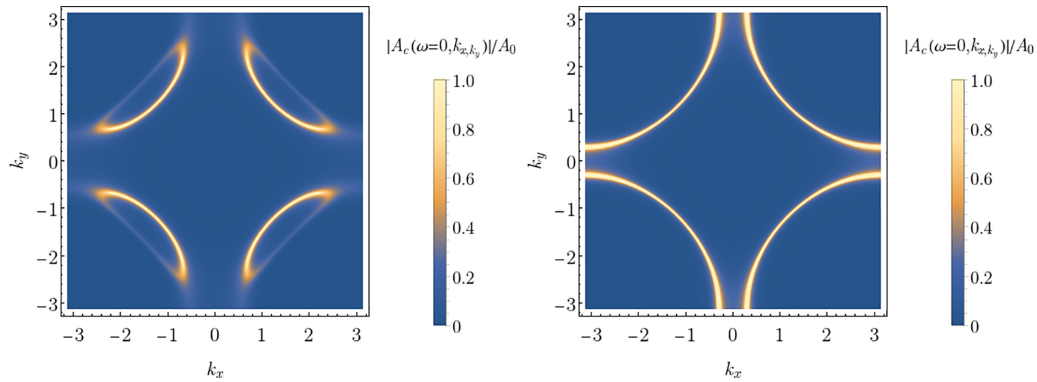

FIG. 9. Spectral weight in the FL* and D phase. Parameters: $\Phi = 0.09, Z = 0.0, \mu_c = -0.24, \mu_f = 0.009$. $\Phi = 0$ in the D phase.

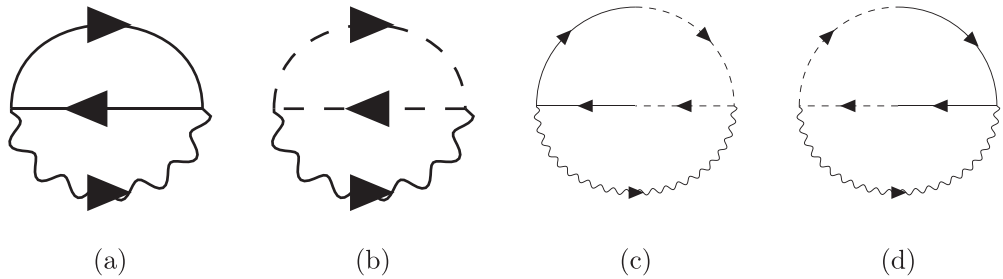

FIG. 10. Self-energy diagrams from the J_s and $J_\perp$ vertices. (a) Diagram from only J_s vertex proportional to J_s^2. (b) Diagram from only $J_\perp$ vertex proportional to $J_\perp^2$. (c),(d) Diagrams combining J_s and $J_\perp$ vertices, which involves the mixed propagators G_{cf} and G_{fc}, and is proportional to $J_s J_\perp$ with an additional suppression by $|\bar{\Phi}|^2$. Solid lines correspond to c propagators, dashed lines correspond to f propagators, and wiggly lines correspond to bare Z boson propagator. The lines that are both solid and dashed correspond to G_{cf} and G_{fc}.

where

$$E_{1\vec{k}} = \frac{\epsilon_{c\vec{k}} + \epsilon_{f\vec{k}} + \sqrt{(\epsilon_{c\vec{k}} - \epsilon_{f\vec{k}})^2 + 4|\bar{\Phi}|^2}}{2},$$
$$E_{2\vec{k}} = \frac{\epsilon_{c\vec{k}} + \epsilon_{f\vec{k}} - \sqrt{(\epsilon_{c\vec{k}} - \epsilon_{f\vec{k}})^2 + 4|\bar{\Phi}|^2}}{2}, \tag{5.11}$$

and $\epsilon_{c\vec{k}}, \epsilon_{f\vec{k}}$ are defined in Eqs. (4.3) and (4.4).

The Z^α are described by a CP^1 field theory,

$$\mathcal{L} = \tfrac{1}{g}|(\partial_\mu - ia_\mu)Z^\alpha|^2 + i\lambda(|Z^\alpha|^2 - 1). \tag{5.12}$$

Here $i\lambda = \bar{\lambda} + i\tilde{\lambda}$, where $\tilde{\lambda}$ is the fluctuating part of λ, and the saddle point $\bar{\lambda}$ is the Lagrange multiplier imposing the constraint on the Z boson density. Thus, ignoring the gauge field, the Z boson Green's function is

$$D(\vec{k}, i\omega) = \frac{g}{\omega^2 + \epsilon_{Z\vec{k}} + \bar{\lambda} - \Pi(\vec{k}, i\omega)}, \tag{5.13}$$

where $\Pi(\vec{k}, i\omega)$ denotes the self-energy of the Z boson. The bare Z boson propagator is given by

$$D^0(\vec{k}, i\omega) = \frac{g}{(i\omega + E_{Z\vec{k}})(-i\omega + E_{Z\vec{k}})}, \tag{5.14}$$

where $E_{Z\vec{k}} = \sqrt{\epsilon_{Z\vec{k}} + \bar{\lambda}}$, with $\epsilon_{Z\vec{k}} = k^2$ in the continuum, but on the lattice we use $\epsilon_{Z\vec{k}} = v\{1 - [\cos(k_x) + \cos(k_y)]/2\}$ leading to the form $\epsilon_{Z\vec{k}} \sim vk^2/4$ near $\vec{k} = 0$. We write the coupling of Z bosons to the c and f layers in the first terms in Eq. (3.4) as

$$H_Z = \sum_i \eta_i Z^*_{i\gamma} \sigma^{a\gamma}_\delta Z^\delta_i \left[-J_s c^\dagger_{i\alpha} \sigma^{a\alpha}_\beta c^\beta_i + J_\perp f^\dagger_{i\alpha} \sigma^{a\alpha}_\beta f^\beta_i\right], \tag{5.15}$$

where we recall that $\eta_i = (-1)^{x_i + y_i}$. In addition, we will also consider the influence of a term of the form

$$H_3 = J_3 \sum_i \eta_i Z^*_{i\gamma} \sigma^{a\gamma}_\delta Z^\delta_i \left[c^\dagger_{i\alpha} \sigma^{a\alpha}_\beta f^\beta_i + f^\dagger_{i\alpha} \sigma^{a\alpha}_\beta c^\beta_i\right]. \tag{5.16}$$

This term involves a nonlocal exchange between the top two layers, and it is clearly permitted by the symmetries of the problem.

The coupling terms in Eqs. (5.15) and (5.16) contribute to self-energy corrections to the Z boson propagator. At the bare level, the Z boson propagator at $i\omega = 0$, $D^0(\vec{k}, i\omega = 0)$, has a maximum at $\vec{k} = 0$. We are interested in the case in which the renormalized Z propagator at $i\omega = 0$, $D(\vec{k}, i\omega = 0)$, has a maximum at $\vec{k} \neq 0$ or, equivalently, the inverse Z propagator $D(\vec{k}, i\omega = 0)^{-1}$ has its minimum at $\vec{k} \neq 0$. This means that at low temperatures, the Z boson can condense at this nonzero $\vec{k}$ leading to a nontrivial spin order. In our case, that may correspond to a spiral or a double spiral.

A. Spinon self-energy

Let us first write the lowest-order self-energy contribution from the H_Z term in Eq. (5.15). It has two diagrams shown in Figs. 10(a) and 10(b) leading to the following forms:

$$\Pi_{10a}(\vec{k}, i\omega) = -\frac{6J_s^2}{\beta^2} \sum_{i\omega_1, i\omega_2} \int_{\vec{k}} G_c(\vec{k}_1, i\omega_1) G_c(\vec{k}_2, i\omega_2) \times D^0(\vec{k} - \vec{k}_1 + \vec{k}_2 - \vec{Q}_\pi, i\omega + i\omega_2 - i\omega_1), \tag{5.17}$$

$$\Pi_{10b}(\vec{k}, i\omega) = -\frac{6J_\perp^2}{\beta^2} \sum_{i\omega_1, i\omega_2} \int_{\vec{k}} G_f(\vec{k}_1, i\omega_1) G_f(\vec{k}_2, i\omega_2) \times D^0(\vec{k} - \vec{k}_1 + \vec{k}_2 - \vec{Q}_\pi, i\omega + i\omega_2 - i\omega_1), \tag{5.18}$$

where we have used a short-hand notation,

$$\int_{\vec{k}} = \frac{1}{(2\pi)^4} \int d\vec{k}_1 d\vec{k}_2, \tag{5.19}$$

and $\vec{Q}_\pi = (\pi, \pi)$, which arises by writing $\eta_i = e^{i\vec{Q}_\pi \cdot \vec{R}_i}$. It turns out that for both of these diagrams, $-\Pi_{10a/b}(\vec{k}, 0)$ has its minimum at $\vec{k} = 0$, and thus $D(\vec{k}, 0)^{-1}_{10ab} = D^0(\vec{k}, 0)^{-1} - \Pi_{10a}(\vec{k}, 0) - \Pi_{10b}(\vec{k}, 0)$ always has its minimum at $\vec{k} = 0$. In addition to these diagrams, there are also self-energy diagrams involving mixed propagators, G_{cf} and G_{fc}, which lead to a minimum at $\vec{k} \neq 0$ in $D(\vec{k}, 0)^{-1}$. The corresponding diagrams are shown in Figs. 10(c) and 10(d). However, these diagrams are suppressed by a factor of $|\bar{\Phi}|^2$ arising in the mixed propagators, which is quite small. So these contributions will always be subdominant compared to the previous diagrams.

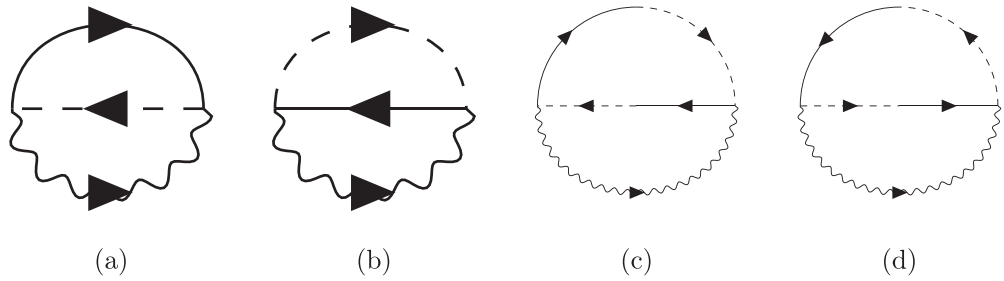

FIG. 11. Self-energy diagrams from the J_3 vertex. Solid lines correspond to c propagators, dashed lines correspond to f propagators, and wiggly lines correspond to bare Z boson propagators. The lines that are both solid and dashed correspond to G_{cf} and G_{fc}.

For completeness, we quote their expressions here,

$$\Pi_{10c}(\vec{k}, i\omega) = \frac{6J_s J_\perp}{\beta^2} \sum_{i\omega_1, i\omega_2} \int_{\vec{k}} G_{cf}(\vec{k}_1, i\omega_1) G_{fc}(\vec{k}_2, i\omega_2) \times D^0(\vec{k} - \vec{k}_1 + \vec{k}_2 - \vec{Q}_\pi, i\omega + i\omega_2 - i\omega_1), \tag{5.20}$$

$$\Pi_{10d}(\vec{k}, i\omega) = \frac{6J_\perp J_s}{\beta^2} \sum_{i\omega_1, i\omega_2} \int_{\vec{k}} G_{fc}(\vec{k}_1, i\omega_1) G_{cf}(\vec{k}_2, i\omega_2) \times D^0(\vec{k} - \vec{k}_1 + \vec{k}_2 - \vec{Q}_\pi, i\omega + i\omega_2 - i\omega_1). \tag{5.21}$$

The self-energy contribution arising from the H_3 term has two diagrams involving normal propagators, shown in Figs. 11(a) and 11(b), giving the following expressions:

$$\Pi_{11a}(\vec{k}, i\omega) = -\frac{6J_3^2}{\beta^2} \sum_{i\omega_1, i\omega_2} \int_{\vec{k}} G_c(\vec{k}_1, i\omega_1) G_f(\vec{k}_2, i\omega_2) \times D^0(\vec{k} - \vec{k}_1 + \vec{k}_2 - \vec{Q}_\pi, i\omega + i\omega_2 - i\omega_1), \tag{5.22}$$

$$\Pi_{11b}(\vec{k}, i\omega) = -\frac{6J_3^2}{\beta^2} \sum_{i\omega_1, i\omega_2} \int_{\vec{k}} G_f(\vec{k}_1, i\omega_1) G_c(\vec{k}_2, i\omega_2) \times D^0(\vec{k} - \vec{k}_1 + \vec{k}_2 - \vec{Q}_\pi, i\omega + i\omega_2 - i\omega_1). \tag{5.23}$$

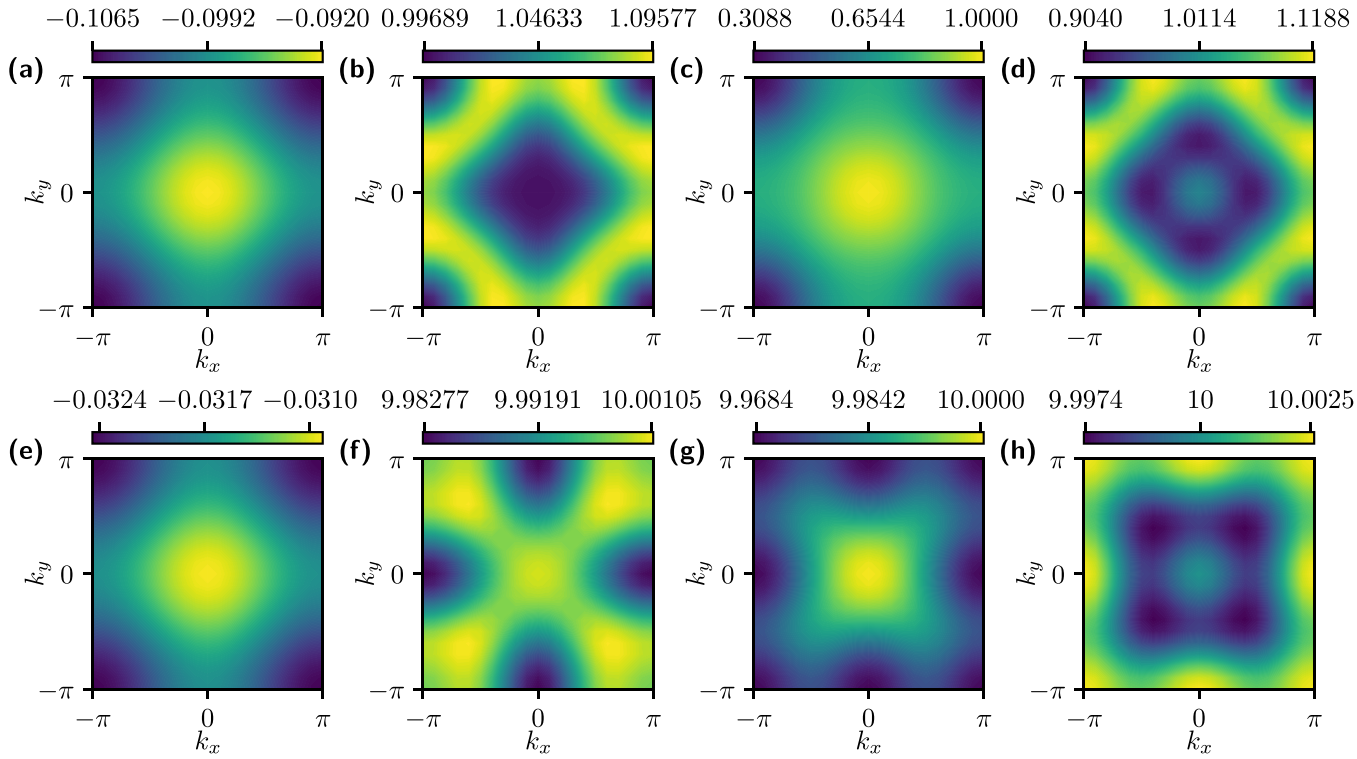

FIG. 12. Self-energy contributions and bosonic propagators. In subfigures (a) and (e) the self-energy contributions $[-\Pi_{11a}(\vec{k}, 0) - \Pi_{11b}(\vec{k}, 0)]/6J_3^2$ are shown for $m_Z^2 = 1,\ \beta = 10$ and $m_Z^2 = 10,\ \beta = 10$, respectively. The remaining subfigures show the inverse propagator of the Z boson $D(\vec{k}, 0)^{-1}_{11ab}$, computed according to Eq. (5.26), at $i\omega = 0$ for different values of J_3, m_Z^2, and β: (b) $m_Z^2 = 1$, $\beta = 10$, $6J_3^2 = 552.5$; (c) $m_Z^2 = 1$, $\beta = 10$, $6J_3^2 = 600$; (d) $m_Z^2 = 1$, $\beta = 1000$, $6J_3^2 = 378$; (f) $m_Z^2 = 10$, $\beta = 10$, $6J_3^2 = 5300$; (g) $m_Z^2 = 10$, $\beta = 10$, $6J_3^2 = 5319$; (h) $m_Z^2 = 10$, $\beta = 5$, $6J_3^2 = 9655$. These values were chosen to showcase different constellations in which the minimum of the inverse boson propagator can occur at $\vec{k} \neq 0$. For the boson dispersion, a value of $v = 4$ was used.

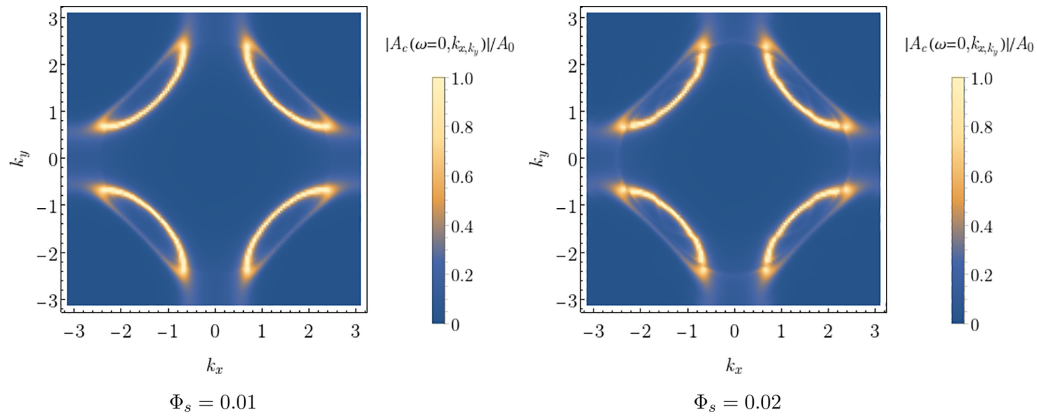

FIG. 13. Spectral weight in the collinear bidirectional SDW. $J_s = 2J_\perp = 1$, $J_3 = 0.2$.

For these diagrams, $-\Pi_{11a/b}$ has its minimum at $\vec{k} \neq 0$ (see Fig. 12) and thus for sufficiently large values of J_3 the inverse propagator of the Z boson, $D(\vec{k},0)^{-1}_{11ab} = D^0(\vec{k},0)^{-1} - \Pi_{11a}(\vec{k},0) - \Pi_{11b}(\vec{k},0)$, has a minimum at $\vec{k} \neq 0$. In addition, as before, there are two more diagrams involving mixed propagators, shown in Figs. 11(c) and 11(d), with the following expressions:

$$\Pi_{11c}(\vec{k}, i\omega) = -\frac{6J_3^2}{\beta^2} \sum_{i\omega_1, i\omega_2} \int_{\vec{k}} G_{cf}(\vec{k}_1, i\omega_1) G_{cf}(\vec{k}_2, i\omega_2) \times D^0(\vec{k} - \vec{k}_1 + \vec{k}_2 - \vec{Q}_\pi, i\omega + i\omega_2 - i\omega_1), \tag{5.24}$$

$$\Pi_{11d}(\vec{k}, i\omega) = -\frac{6J_3^2}{\beta^2} \sum_{i\omega_1, i\omega_2} \int_{\vec{k}} G_{fc}(\vec{k}_1, i\omega_1) G_{fc}(\vec{k}_2, i\omega_2) \times D^0(\vec{k} - \vec{k}_1 + \vec{k}_2 - \vec{Q}_\pi, i\omega + i\omega_2 - i\omega_1). \tag{5.25}$$

These are again suppressed by an additional small factor of $|\bar{\Phi}|^2$ and so these are subdominant compared to the previous diagrams. In Appendix A, we provide detailed expressions of the self-energy terms.

To make the renormalization of the Z boson partially self-consistent, we employ a similar approach to that in Ref. [13]. To this end, we rewrite its propagator defined in Eq. (5.13) as

$$D(\vec{k}, i\omega) = \frac{g}{\omega^2 + \epsilon_{Z\vec{k}} + m_Z^2 - \Pi(\vec{k}, i\omega) + \Pi(0,0)}, \tag{5.26}$$

where $m_Z^2 = \overline{\lambda} - \Pi(0,0)$ is the boson mass gap. Thus, to take into account the renormalized mass gap, in Eq. (5.14) we replace $\overline{\lambda}$ by m_Z^2, effectively using $D^0(\vec{k}, i\omega) = (\omega^2 + \epsilon_{Z\vec{k}} + m_Z^2)^{-1}$ in Eqs. (5.17) and (5.18) and Eqs. (5.20)–(5.25). As a result, the closing of the bosonic mass gap due to the renormalization process affects the renormalization of the Z boson.

In Fig. 12 we show self-energy contributions $[-\Pi_{11a}(\vec{k},0) - \Pi_{11b}(\vec{k},0)]$ (in units of $6J_3^2$) along with the inverse propagator of the Z boson resulting from these corrections. As can be seen, the self-energy contributions (multiplied by a factor of -1) are negative and feature a minimum at $\vec{k} = \vec{Q}_\pi$. Thus, for a sufficiently large value of $6J_3^2$, the Z boson inverse propagator, computed according to Eq. (5.26), features a minimum at $\vec{k} \neq 0$. For smaller values of J_3 its minimum remains at $\vec{k} = 0$, while for intermediate values its minimum can behave in one of several ways before eventually reaching $\vec{k} = \vec{Q}_\pi$ for sufficiently large values of J_3. For these intermediate values of J_3 we have observed instances in which the minimum moved along the diagonal ($k_x = k_y$) or the vertical/horizontal ($k_y = 0/k_x = 0$). Additionally, it has jumped from $\vec{k} = 0$ via $\vec{k} = (\pi, 0)$ to $\vec{k} = \vec{Q}_\pi$ or even directly. Several such possibilities are illustrated in Fig. 12, where we show bosonic propagators with degenerate minima between 0 and $\vec{Q}_\pi$ (b) or $(\pi, 0)$ and (π, π) (g) as well as propagators with minima at $\vec{Q}_\pi$ (c), minima at $(k, 0)$, $(0, k)$ (d), minima at $(\pi, 0)$, $(0, \pi)$ (f), and minima at (k, k) (h), where $k \in [0, \pi]$ and we have only listed minima in the upper right quadrant.

B. Fermi surfaces

This section will briefly present the Fermi surfaces induced by incommensurate SDW order across the transition from the FL* metal. Along with the spiral SDW obtained in (5.6), we will also consider collinear SDW states for completeness in the following subsections. The latter states are "stripes" because they have coexisting charge density wave order.

1. Collinear bidirectional SDW

Collinear SDWs are characterized by complex order parameters Φ_x^a and Φ_y^a, taking the place of the real vectors $m_{1,2}^a$ in (5.6) for spiral SDWs. These determine the spin density via

$$S^a(\mathbf{r}) = \mathrm{Re}\left[e^{i\vec{K}_x\cdot\mathbf{r}}\Phi_x^a(\mathbf{r}) + e^{i\vec{K}_y\cdot\mathbf{r}}\Phi_y^a(\mathbf{r})\right], \tag{5.27}$$

where

$$\vec{K}_x = (3\pi/4, \pi), \quad \vec{K}_y = (\pi, 3\pi/4). \tag{5.28}$$

An order parameter with $\arg(\Phi_{xa}) = (0, \pi/4, \pi/2, 3\pi/4, \pi, 5\pi/4, 3\pi/2, 7\pi/4)$ is bond-centered, and one with $\arg(\Phi_{xa}) = (\pi/8, 3\pi/8, 5\pi/8, 7\pi/8, 9\pi/8, 11\pi/8, 13\pi/8, 15\pi/8)$ is site-centered. We chose a commensurate wave vector to obtain a smaller unit cell.

The mean-field Hamiltonian for the bidirectional SDW will be given by $H_{cf}^a + H_{cf}^c$, with the wave vectors in (5.28). In

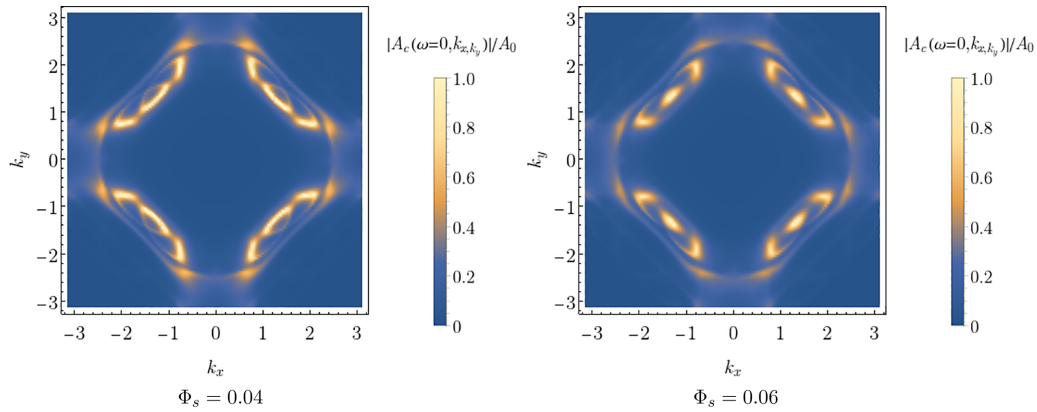

FIG. 14. Spectral weight in the collinear bidirectional SDW. $J_s = 2J_\perp = 1$, $J_3 = 0.2$.

momentum space, H^a_{cf} is given by Eq. (5.8) and H^c_{cf} looks as follows:

$$H^c_{cf} = \sum_{\vec{k}} -J_s\Big(\Phi_x c^\dagger_{\vec{k}+\vec{K}_x,\alpha}\,\sigma^{z\alpha}_{\beta}\,c^\beta_{\vec{k}} + \Phi_y c^\dagger_{\vec{k}+\vec{K}_y,\alpha}\,\sigma^{z\alpha}_{\beta}\,c^\beta_{\vec{k}}\Big) + \text{H.c.} + J_\perp(\cdots) + J_3(\cdots), \tag{5.29}$$

where the $J_\perp$ term is the same as the J_s term with $c \to f$. We also include the J_3 term, which couples c and f fermions in the same way; see (5.16).

The Hamiltonian can be diagonalized in the following basis of 128 elements given by $\Psi_k = (c_{k_x+Q_i,k_y+Q_j}, f_{k_x+Q_i,k_y+Q_j})$, where $Q_i = (0, 3\pi/4, 6\pi/4, 9\pi/4, \pi, 7\pi/4, 2\pi/4, 5\pi/4)$. We can compute a spectral weight after the SDW order emerges. For simplicity, we put $J_s = 2J_\perp = 1$, $J_3 = 0$ and change only $\Phi_x = \Phi_s$, $\Phi_y = \Phi_s e^{i\pi/8}$. Chemical potentials and hybridization were chosen to be as in Fig. 5. Figures 13 and 14 show that hole pockets evolve into more complicated Fermi surfaces with the possible gap closing in the antinodal region.

2. Collinear unidirectional SDW

Now we consider the case of unidirectional SDW with wave vector $\vec{K}_x = (3\pi/4, \pi)$. The Hamiltonian will be the same as in a previous case with $\Phi_y = 0$. The evolution of the spectral weight is depicted in Fig. 15. We see that as we move deeper into the SDW phase, the hole pocket of a different size arises in the nodal region followed by the emergence of the fermion pocket in the antinodal region.

C. Spiral unidirectional SDW

We consider spiral SDW with $\vec{S}(r) = \Phi_x(\vec{x} + i\vec{y})e^{i\vec{K}_x\vec{r}} +$ (c.c.). The H^a_{cf} part of the Hamiltonian is not changed, while the H^c_{cf} part looks as follows:

$$H^c_{cf} = -J_s\Big(\Phi_x c^\dagger_{\vec{k}+\vec{K}_x,\alpha}(\sigma^+)^\alpha_\beta c^\beta_{\vec{k}} + \Phi_x c^\dagger_{\vec{k},\alpha}(\sigma^-)^\alpha_\beta c^\beta_{\vec{k}+\vec{K}_x}\Big) + J_\perp(\cdots) + J_3(\cdots). \tag{5.30}$$

The Hamiltonian can be diagonalized in the following basis:

$$\Psi_{\vec{k}} = (c_{\vec{k},\uparrow}, c_{\vec{k},\downarrow}, c_{\vec{k}+\vec{K}_x,\uparrow}, c_{\vec{k}-\vec{K}_x,\downarrow}, f_{\vec{k},\uparrow}, f_{\vec{k},\downarrow}, f_{\vec{k}+\vec{K}_x,\uparrow}, f_{\vec{k}-\vec{K}_x,\downarrow}). \tag{5.31}$$

It is important to stress that even for incommensurate $\vec{K}_x$, the size of the basis is not changed; that is because fermions with spin up can only scatter by wave vector $+\vec{K}_x$ to fermions with spin down, but cannot scatter back with wave vector $-\vec{K}_x$. So the present computation can be carried out for arbitrary $\vec{K}$, and the results for commensurate and incommensurate wave vectors are not different. The distribution of the spectral weight, see Fig. 16, is similar to a collinear scenario, but the important difference is that original hole pockets do not disappear, and reconstruction of the Fermi surface happens on

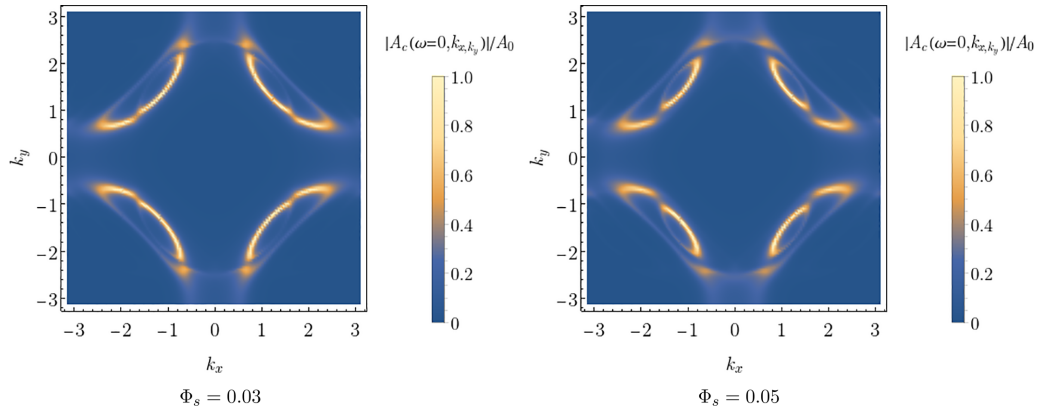

FIG. 15. Spectral weight in the unidirectional collinear SDW phase. $J_s = 2J_\perp = 1$, $J_3 = 0.2$.

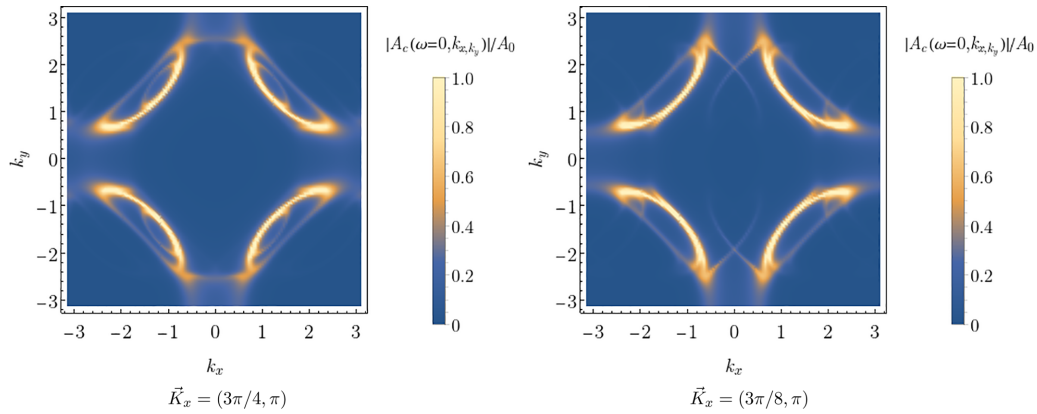

FIG. 16. Spectral weight in the unidirectional spiral SDW phase. $J_s = 2J_\perp = 1$, $J_3 = 0.2$, $\Phi_s = 0.06$.

top of the hole pockets. The exact way the Fermi surface is reconstructed would depend on the wave vector $\vec{K}_x$.

VI. DISCUSSION

An earlier paper [28] showed that the observed photoemission spectrum in the pseudogap metal of the underdoped hole-doped cuprates [7,10] could be well described by a paramagnon fractionalization theory summarized in Figs. 1 and 2. A similar connection to the experimental data has also been made in the YRZ framework [54]. We view this agreement as evidence in favor of the presence of spin fractionalization in the underdoped cuprates at intermediate temperatures.

Also notable are recent experimental studies [78] of the very lightly doped state with long-range Néel order at wave vector (π, π). Convincing evidence has recently been obtained for the presence of hole pockets in such a metallic state.

This situation provided motivation for the studies presented in this paper, as summarized in Fig. 3. We view the pseudogap metal at intermediate temperatures and underdoping as the "parent" of the phase diagram. We described this pseudogap as a metal with hole pockets whose enclosed volume does not equal the Luttinger volume. Consequently, this phase must have fractionalized spin excitations, i.e., it is an FL* metal.

We described how the FL* state of the pseudogap metal evolved into a metallic (π, π) Néel state without fractionalization with *decreasing* doping, as shown by arrow $\mathbb{A}$ in Fig. 3. We used charge-neutral bosonic spinons to represent the fractionalized paramagnons, and condensation of such spinons led to the Néel state in which all emergent gauge fields were Higgsed. We described the evolution of the hole pockets across the transition from the FL* state to the metallic Néel state in Sec. IV B 1. We are presenting these results as predictions for future observations which are able to follow the Fermi surfaces from the pseudogap metal to the ordered Néel state; in particular, Figs. 5 and 6 show how the effective size of the hole pocket doubles [60] in the full Brillouin zone across the transition from the pseudogap metal to the Néel metal. Furthermore, we propose that, in sufficiently clean samples, the evidence for hole pockets in the pseudogap metal state *without* magnetic order will become sharper than that presented in Ref. [11]: this would then constitute direct evidence for an FL* metal with fractionalized excitations.

We also considered the situation with *increasing* doping from the pseudogap metal, as shown by arrow $\mathbb{B}$ in Fig. 3. In this direction, the FL* state evolves into a conventional Fermi liquid via an intermediate metallic state with ghost Fermi surfaces [25–27]. We studied this route to the confinement of fractionalized excitations, and our results are summarized in the phase diagram in Fig. 4. All the phases in this diagram are described in terms of a gauge theory of the fields collected in Table I. The paramagnon field $\boldsymbol{n}$ is gauge-neutral, and it is related to the fractionalized fields via (2.6); the paramagnon becomes an elementary excitation in the Fermi liquid phases where all gauge charges are confined. The effective action for these fields can be deduced from the symmetries listed in Table I, and the potential for the bosonic fields appeared in (3.1). The nature of the transition out of the pseudogap metal to the Fermi liquid, i.e., that between phases A and D in Fig. 4, is the same as that considered in earlier work [25,26], and it involves critical fluctuations of the Higgs field Φ coupled to the c and f Fermi surfaces. The second ancilla layer of spins is not important to this critical theory, and so the use of bosonic spinons here, in contrast to the fermionic spinons in the earlier work [25,26], does not make a substantial difference. Upon adding spatial disorder to the Yukawa coupling of the Higgs field Φ, such a theory will yield a strange metal with linear-T resistivity in the critical region [79,80].

Finally, in Sec. V we considered the fate of the FL* metal upon lowering T within the pseudogap, as shown by arrow $\mathbb{C}$ in Fig. 3. Here, we face the important question of whether the fractionalization will survive at lower T, or even at $T = 0$. There has been no direct experimental evidence in favor of fractionalization at low T so far. Recent numerical studies on the doped Hubbard model [76,77] indicate that the $T = 0$ state is a conventional striped state with both spin and charge density wave orders. In light of this, Sec. V considered the appearance of a confining incommensurate SDW state via the condensation of the bosonic spinons at an incommensurate wave vector. We showed in Sec. V A that coupling of the bosonic spinons to the hole pockets could induce a self-energy so that the spinon dispersion minimum was at an incommensurate wave vector. This mechanism for the appearance of incommensurate SDW from hole pockets is similar to that considered in Ref. [13], although that analysis was expressed

in terms of the paramagnon dispersion. We presented predictions for the photoemission spectrum as it evolved from the pseudogap to incommensurate SDW states.

A significant result of our analysis, appearing in Eqs. (5.1)–(5.7), is that our spinon condensation mechanism did not induce a collinear SDW with coexisting charge stripe order. Instead, the SDWs found in Sec. V carried spiral spin correlations. The basic reasoning is independent of the form of the spinon free energy. These equations show that incommensurate spinons induce an incommensurate SDW *along with* a commensurate SDW. As such a coexistence is not observed, we impose the requirement that the commensurate SDW vanish: we then find that this can only be achieved by an incommensurate spiral SDW.

Arrow $\mathbb{C}$ in Fig. 3 also indicates transitions from FL* to d-wave superconductivity and charge density wave. Such transitions were discussed in Refs. [81,82] using fermionic spinons for cases in which the parent was a $\mathbb{Z}_2$ spin liquid. The dual fermionic spinon description of the confining instabilities of a parent $\mathbb{CP}^1$ U(1) spin liquid is presented in a companion paper [37]; the dual of the $\mathbb{CP}^1$ U(1) spin liquid has fermionic spinons moving in π flux coupled to an emergent SU(2) gauge field [34].

ACKNOWLEDGMENTS

We thank Seamus Davis, Michele Fabrizio, Antoine Georges, Masatoshi Imada, Takeshi Kondo, Peter Johnson, Zhi-Xun Shen, Louis Taillefer, and Ya-Hui Zhang for valuable discussions. This research was supported by the U.S. National Science Foundation Grant No. DMR-2002850 and by the Simons Collaboration on Ultra-Quantum Matter which is a grant from the Simons Foundation (651440, S.S.). J.v.M. is supported by a fellowship of the International Max Planck Research School for Quantum Science and Technology (IMPRS-QST).

APPENDIX: SELF-ENERGY EXPRESSION

We can perform the frequency summation in the self-energy expression in Eq. (5.17), and we obtain

$$\Pi_{10a}(\vec{k}, i\omega) = \frac{6J_s^2}{(2\pi)^4}\int d\vec{k}_1 d\vec{k}_2 d\vec{k}_3\, \delta(\vec{k}_1 - \vec{k}_2 + \vec{k}_3 - \vec{k} + \vec{Q}_\pi) \sum_{i=1}^{12} S_i, \tag{A1}$$

$$S_1 = \frac{n_F(E_{1\vec{k}_1}) n_F(E_{1\vec{k}_2})(E_{1\vec{k}_1} - \epsilon_{f\vec{k}_1})(E_{1\vec{k}_2} - \epsilon_{f\vec{k}_2})}{(i\omega - E_{1\vec{k}_1} + E_{1\vec{k}_2} + E_{Z\vec{k}_3})(i\omega - E_{1\vec{k}_1} + E_{1\vec{k}_2} - E_{Z\vec{k}_3})} \frac{1}{(E_{1\vec{k}_1} - E_{2\vec{k}_1})} \frac{1}{(E_{1\vec{k}_2} - E_{2\vec{k}_2})}, \tag{A2}$$

$$S_2 = \frac{n_F(E_{1\vec{k}_1}) n_F(E_{2\vec{k}_2})(E_{1\vec{k}_1} - \epsilon_{f\vec{k}_1})(E_{2\vec{k}_2} - \epsilon_{f\vec{k}_2})}{(i\omega - E_{1\vec{k}_1} + E_{2\vec{k}_2} + E_{Z\vec{k}_3})(i\omega - E_{1\vec{k}_1} + E_{2\vec{k}_2} - E_{Z\vec{k}_3})} \frac{1}{(E_{1\vec{k}_1} - E_{2\vec{k}_1})} \frac{1}{(E_{2\vec{k}_2} - E_{1\vec{k}_2})}, \tag{A3}$$

$$S_3 = \frac{n_F(E_{2\vec{k}_1}) n_F(E_{1\vec{k}_2})(E_{2\vec{k}_1} - \epsilon_{f\vec{k}_1})(E_{1\vec{k}_2} - \epsilon_{f\vec{k}_2})}{(i\omega - E_{2\vec{k}_1} + E_{1\vec{k}_2} + E_{Z\vec{k}_3})(i\omega - E_{2\vec{k}_1} + E_{1\vec{k}_2} - E_{Z\vec{k}_3})} \frac{1}{(E_{2\vec{k}_1} - E_{1\vec{k}_1})} \frac{1}{(E_{1\vec{k}_2} - E_{2\vec{k}_2})}, \tag{A4}$$

$$S_4 = \frac{n_F(E_{2\vec{k}_1}) n_F(E_{2\vec{k}_2})(E_{2\vec{k}_1} - \epsilon_{f\vec{k}_1})(E_{2\vec{k}_2} - \epsilon_{f\vec{k}_2})}{(i\omega - E_{2\vec{k}_1} + E_{2\vec{k}_2} + E_{Z\vec{k}_3})(i\omega - E_{2\vec{k}_1} + E_{2\vec{k}_2} - E_{Z\vec{k}_3})} \frac{1}{(E_{2\vec{k}_1} - E_{1\vec{k}_1})} \frac{1}{(E_{2\vec{k}_2} - E_{1\vec{k}_2})}, \tag{A5}$$

$$S_5 = -\frac{(E_{1\vec{k}_2} - \epsilon_{f\vec{k}_2})}{2E_{Z\vec{k}_3}(E_{1\vec{k}_2} - E_{2\vec{k}_2})} \frac{n_F(E_{1\vec{k}_2}) n_B(E_{Z\vec{k}_3})(i\omega - \epsilon_{f\vec{k}_1} + E_{1\vec{k}_2} + E_{Z\vec{k}_3})}{(i\omega - E_{1\vec{k}_1} + E_{1\vec{k}_2} + E_{Z\vec{k}_3})(i\omega - E_{2\vec{k}_1} + E_{1\vec{k}_2} + E_{Z\vec{k}_3})}, \tag{A6}$$

$$S_6 = -\frac{(E_{2\vec{k}_2} - \epsilon_{f\vec{k}_2})}{2E_{Z\vec{k}_3}(E_{2\vec{k}_2} - E_{1\vec{k}_2})} \frac{n_F(E_{2\vec{k}_2}) n_B(E_{Z\vec{k}_3})(i\omega - \epsilon_{f\vec{k}_1} + E_{2\vec{k}_2} + E_{Z\vec{k}_3})}{(i\omega - E_{1\vec{k}_1} + E_{2\vec{k}_2} + E_{Z\vec{k}_3})(i\omega - E_{2\vec{k}_1} + E_{2\vec{k}_2} + E_{Z\vec{k}_3})}, \tag{A7}$$

$$S_7 = \frac{(E_{1\vec{k}_2} - \epsilon_{f\vec{k}_2})}{2E_{Z\vec{k}_3}(E_{1\vec{k}_2} - E_{2\vec{k}_2})} \frac{n_F(E_{1\vec{k}_2}) n_B(-E_{Z\vec{k}_3})(i\omega - \epsilon_{f\vec{k}_1} + E_{1\vec{k}_2} - E_{Z\vec{k}_3})}{(i\omega - E_{1\vec{k}_1} + E_{1\vec{k}_2} - E_{Z\vec{k}_3})(i\omega - E_{2\vec{k}_1} + E_{1\vec{k}_2} - E_{Z\vec{k}_3})}, \tag{A8}$$

$$S_8 = \frac{(E_{2\vec{k}_2} - \epsilon_{f\vec{k}_2})}{2E_{Z\vec{k}_3}(E_{2\vec{k}_2} - E_{1\vec{k}_2})} \frac{n_F(E_{2\vec{k}_2}) n_B(-E_{Z\vec{k}_3})(i\omega - \epsilon_{f\vec{k}_1} + E_{2\vec{k}_2} - E_{Z\vec{k}_3})}{(i\omega - E_{1\vec{k}_1} + E_{2\vec{k}_2} - E_{Z\vec{k}_3})(i\omega - E_{2\vec{k}_1} + E_{2\vec{k}_2} - E_{Z\vec{k}_3})}, \tag{A9}$$

$$S_9 = \frac{(E_{1\vec{k}_1} - \epsilon_{f\vec{k}_1})}{2E_{Z\vec{k}_3}(E_{1\vec{k}_1} - E_{2\vec{k}_1})} \frac{n_F(E_{1\vec{k}_1} - E_{Z\vec{k}_3})[n_F(E_{1\vec{k}_1}) + n_B(E_{Z\vec{k}_3})](i\omega - E_{1\vec{k}_1} + \epsilon_{f\vec{k}_2} + E_{Z\vec{k}_3})}{(i\omega - E_{1\vec{k}_1} + E_{1\vec{k}_2} + E_{Z\vec{k}_3})(i\omega - E_{1\vec{k}_1} + E_{2\vec{k}_2} + E_{Z\vec{k}_3})}, \tag{A10}$$

$$S_{10} = -\frac{n_F(E_{1\vec{k}_1} + E_{Z\vec{k}_3})[n_F(E_{1\vec{k}_1}) + n_B(-E_{Z\vec{k}_3})](i\omega - E_{1\vec{k}_1} + \epsilon_{f\vec{k}_2} - E_{Z\vec{k}_3})(E_{1\vec{k}_1} - \epsilon_{f\vec{k}_1})}{2E_{Z\vec{k}_3}(E_{1\vec{k}_1} - E_{2\vec{k}_1})(i\omega - E_{1\vec{k}_1} + E_{1\vec{k}_2} - E_{Z\vec{k}_3})(i\omega - E_{1\vec{k}_1} + E_{2\vec{k}_2} - E_{Z\vec{k}_3})}, \tag{A11}$$

$$S_{11} = \frac{n_F(E_{2\vec{k}_1} - E_{Z\vec{k}_3})[n_F(E_{2\vec{k}_1}) + n_B(E_{Z\vec{k}_3})](i\omega - E_{2\vec{k}_1} + \epsilon_{f\vec{k}_2} + E_{Z\vec{k}_3})(E_{2\vec{k}_1} - \epsilon_{f\vec{k}_1})}{2E_{Z\vec{k}_3}(E_{2\vec{k}_1} - E_{1\vec{k}_1})(i\omega - E_{2\vec{k}_1} + E_{1\vec{k}_2} + E_{Z\vec{k}_3})(i\omega - E_{2\vec{k}_1} + E_{2\vec{k}_2} + E_{Z\vec{k}_3})}, \tag{A12}$$

$$S_{12} = -\frac{n_F(E_{2\vec{k}_1} + E_{Z\vec{k}_3})[n_F(E_{2\vec{k}_1}) + n_B(-E_{Z\vec{k}_3})](i\omega - E_{2\vec{k}_1} + \epsilon_{f\vec{k}_2} - E_{Z\vec{k}_3})(E_{2\vec{k}_1} - \epsilon_{f\vec{k}_1})}{2E_{Z\vec{k}_3}(E_{2\vec{k}_1} - E_{1\vec{k}_1})(i\omega - E_{2\vec{k}_1} + E_{1\vec{k}_2} - E_{Z\vec{k}_3})(i\omega - E_{2\vec{k}_1} + E_{2\vec{k}_2} - E_{Z\vec{k}_3})}. \tag{A13}$$

The expression for the self-energy Π_{10b} in Eq. (5.18) is obtained by replacing $\epsilon_f \to \epsilon_c$ and $J_s \to J_\perp$ in the above expressions. The expression for the self-energy Π_{11a} in Eq. (5.22) is obtained by replacing $\epsilon_{f\vec{k}_2} \to \epsilon_{c\vec{k}_2}$ and $J_s \to J_3$ in the above expressions, while that for Π_{11b} in Eq. (5.23) is obtained by replacing $\epsilon_{f\vec{k}_1} \to \epsilon_{c\vec{k}_1}$ and $J_s \to J_3$. The expressions for the self-energies Π_{10c}, Π_{10d} in Eqs. (5.20) and (5.21) are obtained by replacing all terms in the numerator not involving the Bose- or Fermi-distribution functions by $|\bar{\Phi}|^2$, and replacing $J_s^2 \to J_s J_\perp$ in the above expressions. The expressions for Π_{11c}, Π_{11d} in Eqs. (5.24) and (5.24) are obtained analogously, replacing $J_s \to J_3$.

[1] N. F. Berk and J. R. Schrieffer, Effect of Ferromagnetic Spin Correlations on Superconductivity, Phys. Rev. Lett. **17**, 433 (1966).

[2] S. Doniach and S. Engelsberg, Low-Temperature Properties of Nearly Ferromagnetic Fermi Liquids, Phys. Rev. Lett. **17**, 750 (1966).

[3] D. Vollhardt and P. Wolfle, *The Superfluid Phases of Helium 3*, Dover Books on Physics Series (Dover, 2013).

[4] D. Scalapino, The case of $d_{x^2-y^2}$ pairing in the cuprate superconductors, Phys. Rep. **250**, 329 (1995).

[5] A. V. Chubukov, Pairing mechanism in Fe-based superconductors, Annu. Rev. Condens. Matter Phys. **3**, 57 (2012).

[6] K. M. Shen, F. Ronning, D. H. Lu, F. Baumberger, N. J. C. Ingle, W. S. Lee, W. Meevasana, Y. Kohsaka, M. Azuma, M. Takano, H. Takagi, and Z.-X. Shen, Nodal quasiparticles and antinodal charge ordering in $Ca_{2-x}Na_xCuO_2Cl_2$, Science **307**, 901 (2005).

[7] R.-H. He, M. Hashimoto, H. Karapetyan, J. D. Koralek, J. P. Hinton, J. P. Testaud, V. Nathan, Y. Yoshida, H. Yao, K. Tanaka, W. Meevasana, R. G. Moore, D. H. Lu, S. K. Mo, M. Ishikado, H. Eisaki, Z. Hussain, T. P. Devereaux, S. A. Kivelson, J. Orenstein *et al.*, From a single-band metal to a high-temperature superconductor via two thermal phase transitions, Science **331**, 1579 (2011).

[8] Y. He, Y. Yin, M. Zech, A. Soumyanarayanan, M. M. Yee, T. Williams, M. C. Boyer, K. Chatterjee, W. D. Wise, I. Zeljkovic, T. Kondo, T. Takeuchi, H. Ikuta, P. Mistark, R. S. Markiewicz, A. Bansil, S. Sachdev, E. W. Hudson, and J. E. Hoffman, Fermi surface and pseudogap evolution in a cuprate superconductor, Science **344**, 608 (2014).

[9] K. Fujita, C. K. Kim, I. Lee, J. Lee, M. H. Hamidian, I. A. Firmo, S. Mukhopadhyay, H. Eisaki, S. Uchida, M. J. Lawler, E. A. Kim, and J. C. Davis, Simultaneous transitions in cuprate momentum-space topology and electronic symmetry breaking, Science **344**, 612 (2014).

[10] S.-D. Chen, M. Hashimoto, Y. He, D. Song, K.-J. Xu, J.-F. He, T. P. Devereaux, H. Eisaki, D.-H. Lu, J. Zaanen, and Z.-X. Shen, Incoherent strange metal sharply bounded by a critical doping in Bi2212, Science **366**, 1099 (2019).

[11] H.-B. Yang, J. D. Rameau, Z.-H. Pan, G. D. Gu, P. D. Johnson, H. Claus, D. G. Hinks, and T. E. Kidd, Reconstructed Fermi Surface of Underdoped $Bi_2Sr_2CaCu_2O_{8+\delta}$ Cuprate Superconductors, Phys. Rev. Lett. **107**, 047003 (2011).

[12] Y. Fang, G. Grissonnanche, A. Legros, S. Verret, F. Laliberté, C. Collignon, A. Ataei, M. Dion, J. Zhou, D. Graf, M. J. Lawler, P. A. Goddard, L. Taillefer, and B. J. Ramshaw, Fermi surface transformation at the pseudogap critical point of a cuprate superconductor, Nat. Phys. **18**, 558 (2022).

[13] S. Sachdev, Quantum phases of the Shraiman-Siggia model, Phys. Rev. B **49**, 6770 (1994).

[14] T. Senthil, S. Sachdev, and M. Vojta, Fractionalized Fermi Liquids, Phys. Rev. Lett. **90**, 216403 (2003).

[15] T. Senthil, M. Vojta, and S. Sachdev, Weak magnetism and non-Fermi liquids near heavy-fermion critical points, Phys. Rev. B **69**, 035111 (2004).

[16] Y. Qi and S. Sachdev, Effective theory of Fermi pockets in fluctuating antiferromagnets, Phys. Rev. B **81**, 115129 (2010).

[17] E. G. Moon and S. Sachdev, Underdoped cuprates as fractionalized Fermi liquids: Transition to superconductivity, Phys. Rev. B **83**, 224508 (2011).

[18] M. Punk and S. Sachdev, Fermi surface reconstruction in hole-doped t-J models without long-range antiferromagnetic order, Phys. Rev. B **85**, 195123 (2012).

[19] S. Sachdev, H. D. Scammell, M. S. Scheurer, and G. Tarnopolsky, Gauge theory for the cuprates near optimal doping, Phys. Rev. B **99**, 054516 (2019).

[20] N. Read and S. Sachdev, Valence-Bond and Spin-Peierls Ground States of Low-Dimensional Quantum Antiferromagnets, Phys. Rev. Lett. **62**, 1694 (1989).

[21] N. Read and S. Sachdev, Spin-Peierls, valence-bond solid, and Néel ground states of low-dimensional quantum antiferromagnets, Phys. Rev. B **42**, 4568 (1990).

[22] T. C. Ribeiro and X.-G. Wen, Doped carrier formulation and mean-field theory of the $tt't''$-J model, Phys. Rev. B **74**, 155113 (2006).

[23] T. Senthil, A. Vishwanath, L. Balents, S. Sachdev, and M. P. A. Fisher, Deconfined quantum critical points, Science **303**, 1490 (2004).

[24] T. Senthil, L. Balents, S. Sachdev, A. Vishwanath, and M. P. A. Fisher, Quantum criticality beyond the Landau-Ginzburg-Wilson paradigm, Phys. Rev. B **70**, 144407 (2004).

[25] Y.-H. Zhang and S. Sachdev, From the pseudogap metal to the Fermi liquid using ancilla qubits, Phys. Rev. Res. **2**, 023172 (2020).

[26] Y.-H. Zhang and S. Sachdev, Deconfined criticality and ghost Fermi surfaces at the onset of antiferromagnetism in a metal, Phys. Rev. B **102**, 155124 (2020).

[27] A. Nikolaenko, M. Tikhanovskaya, S. Sachdev, and Y.-H. Zhang, Small to large Fermi surface transition in a single-band model using randomly coupled ancillas, Phys. Rev. B **103**, 235138 (2021).

[28] E. Mascot, A. Nikolaenko, M. Tikhanovskaya, Y.-H. Zhang, D. K. Morr, and S. Sachdev, Electronic spectra with paramagnon fractionalization in the single-band Hubbard model, Phys. Rev. B **105**, 075146 (2022).

[29] N. Lanatà, T.-H. Lee, Y. Yao, and V. Dobrosavljević, Emergent Bloch excitations in mott matter, Phys. Rev. B **96**, 195126 (2017).

[30] M. S. Frank, T.-H. Lee, G. Bhattacharyya, P. K. H. Tsang, V. L. Quito, V. Dobrosavljević, O. Christiansen, and N. Lanatà,

Quantum embedding description of the Anderson lattice model with the ghost Gutzwiller approximation, Phys. Rev. B **104**, L081103 (2021).
[31] D. Guerci, M. Capone, and M. Fabrizio, Exciton Mott transition revisited, Phys. Rev. Mater. **3**, 054605 (2019).
[32] J. R. Moreno, G. Carleo, A. Georges, and J. Stokes, Fermionic wave functions from neural-network constrained hidden states, Proc. Natl. Acad. Sci. (USA) **119**, e2122059119 (2022).
[33] D. P. Arovas and A. Auerbach, Functional integral theories of low-dimensional quantum heisenberg models, Phys. Rev. B **38**, 316 (1988).
[34] C. Wang, A. Nahum, M. A. Metlitski, C. Xu, and T. Senthil, Deconfined Quantum Critical Points: Symmetries and Dualities, Phys. Rev. X **7**, 031051 (2017).
[35] T. Senthil, D. T. Son, C. Wang, and C. Xu, Duality between (2+1) D quantum critical points, Phys. Rep. **827**, 1 (2019).
[36] S. Sachdev, *Quantum Phases of Matter* (Cambridge University Press, Cambridge, UK, 2023).
[37] M. Christos, Z.-X. Luo, H. Shackleton, Y.-H. Zhang, M. Scheurer, and S. Sachdev, A model of d-wave superconductivity, antiferromagnetism, and charge order on the square lattice, Proc. Natl. Acad. Sci. (USA) **120**, e2302701120 (2023).
[38] F. H. L. Essler and A. M. Tsvelik, Weakly coupled one-dimensional Mott insulators, Phys. Rev. B **65**, 115117 (2002).
[39] I. Dzyaloshinskii, Some consequences of the Luttinger theorem: The Luttinger surfaces in non-Fermi liquids and Mott insulators, Phys. Rev. B **68**, 085113 (2003).
[40] T. D. Stanescu and G. Kotliar, Fermi arcs and hidden zeros of the Green function in the pseudogap state, Phys. Rev. B **74**, 125110 (2006).
[41] C. Berthod, T. Giamarchi, S. Biermann, and A. Georges, Breakup of the Fermi Surface Near the Mott Transition in Low-Dimensional Systems, Phys. Rev. Lett. **97**, 136401 (2006).
[42] S. Sakai, Y. Motome, and M. Imada, Evolution of Electronic Structure of Doped Mott Insulators: Reconstruction of Poles and Zeros of Green's Function, Phys. Rev. Lett. **102**, 056404 (2009).
[43] S. Sakai, Y. Motome, and M. Imada, Doped high-T_c cuprate superconductors elucidated in the light of zeros and poles of the electronic Green's function, Phys. Rev. B **82**, 134505 (2010).
[44] S. Sakai, S. Blanc, M. Civelli, Y. Gallais, M. Cazayous, M.-A. Méasson, J. S. Wen, Z. J. Xu, G. D. Gu, G. Sangiovanni, Y. Motome, K. Held, A. Sacuto, A. Georges, and M. Imada, Raman-Scattering Measurements and Theory of the Energy-Momentum Spectrum for Underdoped $Bi_2Sr_2CaCuO_{8+\delta}$ Superconductors: Evidence of an s-Wave Structure for the Pseudogap, Phys. Rev. Lett. **111**, 107001 (2013).
[45] S. Sakai, M. Civelli, and M. Imada, Hidden Fermionic Excitation Boosting High-Temperature Superconductivity in Cuprates, Phys. Rev. Lett. **116**, 057003 (2016).
[46] S. Sakai, M. Civelli, and M. Imada, Direct connection between Mott insulators and d-wave high-temperature superconductors revealed by continuous evolution of self-energy poles, Phys. Rev. B **98**, 195109 (2018).
[47] M. Imada and T. J. Suzuki, Excitons and Dark Fermions as origins of Mott gap, Pseudogap and superconductivity in cuprate superconductors—general concept and basic formalism based on gap physics, J. Phys. Soc. Jpn. **88**, 024701 (2019).
[48] Y. Yamaji, T. Yoshida, A. Fujimori, and M. Imada, Hidden self-energies as origin of cuprate superconductivity revealed by machine learning, Phys. Rev. Res. **3**, 043099 (2021).
[49] M. Imada, Charge order and superconductivity as competing brothers in cuprate high-T_c superconductors, J. Phys. Soc. Jpn. **90**, 111009 (2021).
[50] M. Fabrizio, Landau-Fermi liquids without quasiparticles, Phys. Rev. B **102**, 155122 (2020).
[51] M. Fabrizio, Emergent quasiparticles at Luttinger surfaces, Nat. Commun. **13**, 1561 (2022).
[52] J. Skolimowski and M. Fabrizio, Luttinger's theorem in the presence of Luttinger surfaces, Phys. Rev. B **106**, 045109 (2022).
[53] K.-Y. Yang, T. M. Rice, and F.-C. Zhang, Phenomenological theory of the pseudogap state, Phys. Rev. B **73**, 174501 (2006).
[54] N. J. Robinson, P. D. Johnson, T. M. Rice, and A. M. Tsvelik, Anomalies in the pseudogap phase of the cuprates: Competing ground states and the role of Umklapp scattering, Rep. Prog. Phys. **82**, 126501 (2019).
[55] M. S. Scheurer, S. Chatterjee, W. Wu, M. Ferrero, A. Georges, and S. Sachdev, Topological order in the pseudogap metal, Proc. Natl. Acad. Sci. (USA) **115**, E3665 (2018).
[56] A. V. Chubukov, T. Senthil, and S. Sachdev, Universal Magnetic Properties of Frustrated Quantum Antiferromagnets in Two Dimensions, Phys. Rev. Lett. **72**, 2089 (1994).
[57] P. A. Lee, Gauge Field, Aharonov-Bohm Flux, and High-T_c superconductivity, Phys. Rev. Lett. **63**, 680 (1989).
[58] X.-G. Wen and P. A. Lee, Theory of Underdoped Cuprates, Phys. Rev. Lett. **76**, 503 (1996).
[59] J.-W. Mei, S. Kawasaki, G.-Q. Zheng, Z.-Y. Weng, and X.-G. Wen, Luttinger-volume violating Fermi liquid in the pseudogap phase of the cuprate superconductors, Phys. Rev. B **85**, 134519 (2012).
[60] R. K. Kaul, A. Kolezhuk, M. Levin, S. Sachdev, and T. Senthil, Hole dynamics in an antiferromagnet across a deconfined quantum critical point, Phys. Rev. B **75**, 235122 (2007).
[61] R. K. Kaul, Y. B. Kim, S. Sachdev, and T. Senthil, Algebraic charge liquids, Nat. Phys. **4**, 28 (2008).
[62] S. Sachdev, Topological order, emergent gauge fields, and Fermi surface reconstruction, Rep. Prog. Phys. **82**, 014001 (2019).
[63] P. M. Bonetti and W. Metzner, SU(2) gauge theory of the pseudogap phase in the two-dimensional Hubbard model, Phys. Rev. B **106**, 205152 (2022).
[64] I. Affleck, Z. Zou, T. Hsu, and P. W. Anderson, SU(2) gauge symmetry of the large-U limit of the Hubbard model, Phys. Rev. B **38**, 745 (1988).
[65] S. Sachdev, M. A. Metlitski, Y. Qi, and C. Xu, Fluctuating spin density waves in metals, Phys. Rev. B **80**, 155129 (2009).
[66] P. Coleman, New approach to the mixed-valence problem, Phys. Rev. B **29**, 3035 (1984).
[67] N. Read and D. M. Newns, On the solution of the Coqblin-Schreiffer Hamiltonian by the large-N expansion technique, J. Phys. C **16**, 3273 (1983).
[68] A. Auerbach and K. Levin, Kondo Bosons and the Kondo Lattice: Microscopic Basis for the Heavy Fermi Liquid, Phys. Rev. Lett. **57**, 877 (1986).

[69] A. J. Millis and P. A. Lee, Large-orbital-degeneracy expansion for the lattice Anderson model, Phys. Rev. B **35**, 3394 (1987).

[70] H. Shackleton, A. Thomson, and S. Sachdev, Deconfined criticality and a gapless $\mathbb{Z}_2$ spin liquid in the square-lattice antiferromagnet, Phys. Rev. B **104**, 045110 (2021).

[71] L. Balents and S. Sachdev, Dual vortex theory of doped Mott insulators, Ann. Phys. **322**, 2635 (2007).

[72] D. R. Nelson, J. M. Kosterlitz, and M. E. Fisher, Renormalization-Group Analysis of Bicritical and Tetracritical Points, Phys. Rev. Lett. **33**, 813 (1974).

[73] J. M. Kosterlitz, D. R. Nelson, and M. E. Fisher, Bicritical and tetracritical points in anisotropic antiferromagnetic systems, Phys. Rev. B **13**, 412 (1976).

[74] J. A. Hertz, Quantum critical phenomena, Phys. Rev. B **14**, 1165 (1976).

[75] S.-S. Lee, Stability of the U(1) spin liquid with a spinon Fermi surface in 2+1 dimensions, Phys. Rev. B **78**, 085129 (2008).

[76] B. Xiao, Y.-Y. He, A. Georges, and S. Zhang, Temperature Dependence of Spin and Charge Orders in the Doped Two-Dimensional Hubbard Model, Phys. Rev. X **13**, 011007 (2023).

[77] F. Simkovic, R. Rossi, A. Georges, and M. Ferrero, Origin and fate of the pseudogap in the doped Hubbard model, arXiv:2209.09237.

[78] S. Kunisada, S. Isono, Y. Kohama, S. Sakai, C. Bareille, S. Sakuragi, R. Noguchi, K. Kurokawa, K. Kuroda, Y. Ishida, S. Adachi, R. Sekine, T. K. Kim, C. Cacho, S. Shin, T. Tohyama, K. Tokiwa, and T. Kondo, Observation of small Fermi pockets protected by clean CuO_2 sheets of a high-T_c superconductor, Science **369**, 833 (2020).

[79] E. E. Aldape, T. Cookmeyer, A. A. Patel, and E. Altman, Solvable theory of a strange metal at the breakdown of a heavy Fermi liquid, Phys. Rev. B **105**, 235111 (2022).

[80] A. A. Patel, H. Guo, I. Esterlis, and S. Sachdev, Universal theory of strange metals from spatially random interactions, arXiv:2203.04990 [Science (to be published)].

[81] S. Chatterjee, Y. Qi, S. Sachdev, and J. Steinberg, Superconductivity from a confinement transition out of a fractionalized Fermi liquid with Z_2 topological and Ising-nematic orders, Phys. Rev. B **94**, 024502 (2016).

[82] S. Chatterjee and S. Sachdev, Fractionalized Fermi liquid with Bosonic chargons as a candidate for the pseudogap metal, Phys. Rev. B **94**, 205117 (2016).